Permanent and Transient Upstream Effects in Nonlinear Stratified Flow over a Ridge

STEPHEN T. GARNER

Geophysical Fluid Dynamics Laboratory/NOAA, Princeton, New Jersey

(Manuscript received 21 June 1993, in final form 9 June 1994)

ABSTRACT

The "high drag" state of stratified flow over isolated terrain is still an impediment to theoretical and experimental estimation of topographic wave drag and mean-flow modification. Linear theory misses the transition to the asymmetrical configuration that produces the enhanced drag. Steady-state nonlinear models rely on an ad hoc upstream condition like Long's hypothesis and can, as a result, be inconsistent with the flow established naturally by transients, especially if blocking is involved. Numerical solutions of the stratified initial value problem have left considerable uncertainty about the upstream alteration, especially as regards its permanence.

A time-dependent numerical model with open boundaries is used in an effort to distinguish between permanent and transient upstream flow changes and to relate these to developments near the mountain. A nonrotating atmosphere with initially uniform wind and static stability is assumed. It is found that permanent alterations are primarily due to an initial surge not directly related to wave breaking. Indeed, there are no obvious parameter thresholds in the time-mean upstream state until "orographic adjustment" (deep blocking) commences. Wave breaking, in addition to establishing the downstream shooting flow, generates a persistent, quasi-periodic, upstream transience, which apparently involves the ducting properties of the downslope mixed region. This transience is slow enough to be easily confused with permanent changes.

To understand the inflow alteration and transience, the energy and momentum budgets are examined in regions near the mountain. High drag conditions require permanent changes in flow force difference across the mountain and, consequently, an ongoing horizontal flux of energy and negative momentum. The source of the upstream transience is localized at the head of the mixed region. Blocking allows the total drag to exceed the saturation value by more than an order of magnitude. The implications for nonlinear steady-state models and wave drag parameterization are discussed.

1. Introduction

The theory of stratified, high-drag flow over isolated terrain has borrowed much of its terminology from single-layer hydraulic theory: surge, jump, upstream influence, and wave breaking are familiar terms in both contexts. However, numerical modeling has shown that the stratified phenomenon is more complicated than the hydraulic analog, even in the case of uniform environmental wind, static stability, and density. This has a lot to do with the fact that internal waves are more complicated than surface waves. The present study of the continuously stratified problem has two main goals: 1) to clarify the relationship discussed by Pierrehumbert and Wyman (1985) between wave breaking and permanent upstream changes, and 2) to assess the impact of upstream influence on steady-state models like that proposed by Smith (1985). Both issues relate to the practical problem of estimating wave drag from large-scale conditions.

Corresponding author address: Dr. Stephen Garner, Geophysical Fluid Dynamics Laboratory, P.O. Box 308, Princeton University, Princeton, NJ 08542.

In their numerical study of stratified flow over a ridge, Pierrehumbert and Wyman (1985, hereafter PW) argue that "columnar modes" excited by wave breaking are directly responsible for the permanently decelerated layers of fluid that stretch far upstream along the ground from the mountain. Direct causality between wave breaking and "upstream influence" (permanent changes in the inflow) contrasts with hydraulic models, which produce upstream surges without lee waves (as noted by PW), and with laboratory experiments on stratified, finite-depth fluids, which produce upstream influence, including blocking, without wave breaking (Baines 1979). Conversely, in a numerical study of anelastic mountain waves, Bacmeister and Schoeberl (1989) find that high-level overturning produces no significant, permanent changes in the background flow despite a vigorous wave breaking signal.

The connection between wave breaking and upstream influence is worth clarifying, since, if PW are correct, additional importance would attach to the way in which experiments and theories treat wave-induced instability. The uncertainty stems mainly from the fact that both the wave breaking process and the initialization of the wind across the terrain can produce low-frequency transients with upstream-directed group/phase velocity. Thus, Laprise and Peltier (1989a) dis-

tinguish between "the columnar transients that might be generated by impulsive start-up and the process that leads to the formation of the downslope windstorm." These two processes correspond to the "initial surge" and the "wave breaking surge" in PW's discussion, since the development of severe downslope winds is directly related to the wave breaking. Pierrehumbert and Wyman avoid "wave breaking surge" in favor of "initial surge" when describing solutions with blocking; however, they do not attempt to clarify this difference or the one proposed between the "near mountain" and "far upstream" disturbance.

The uncertainty about the long-range effects of wave breaking is compounded by the difficulty of distinguishing experimentally between temporary and permanent changes due to transients. Thus, Scinocca and Peltier (1989, hereafter SP), concentrating on the downstream disturbances, point out that simulations should continue long past the transition to high drag. It appears that even longer experiments than theirs are now needed to characterize the slow *upstream* transience. Such simulations are feasible if one gives up trying to resolve the extremely small-scale downstream transience highlighted by SP.

Upstream influence also impacts steady-state nonlinear models. The nonlinear model developed by Smith (1985) makes progress by assuming an idealized vertical structure above the terrain and uniform flow profiles far upstream. The latter assumption is a reasonable way to study slowly varying initial wind and static stability *if there is no significant upstream influence* (Long's hypothesis). However, if the incident conditions are permanently altered during a start-up process, as suggested by studies like PW's, not only wave drag estimates but most other characterizations based on Long's hypothesis are suspect. Ideally, the severe wind state should be studied as a development from initial conditions. A gradual start-up of the wind is the most realistic way, but an impulsive start-up (to be used here) has the advantage of comparability with past work. In the interest of realism, one should then focus on the long-timescale transience and ignore timescales on the order of only minutes.[1]

In some studies (e.g., Clark and Peltier 1984; Bacmeister and Pierrehumbert 1988), high drag conditions are determined by the existence of an environmental critical level. Here, we will consider only the more rudimentary case of an initially unsheared, uniformly stratified environment, where mountain amplitude is the sole determining factor in the development of high drag. High-level wave breaking over short obstacles is avoided by assuming incompressible flow. Although Kim and Arakawa (1990) find that wave breaking may involve nonhydrostatic gravity waves to a significant degree, we focus on mountains that are broad enough to produce nearly hydrostatic disturbances. Miranda and James (1992) describe a reverse transition from high to low drag that occurs as the mountain becomes high enough to split the low-level flow. We ignore this possibility by working in a two-dimensional framework.

Time-dependent models using fixed or reentrant upstream boundary conditions (e.g., Bacmeister and Pierrehumbert 1988; Bacmeister and Schoeberl 1989) can provide only limited indications about mean-flow modification. The present study relies on new, long-term numerical integrations with open boundaries. Spurious boundary reflections and sources are unacceptable in an investigation of steady states or long-term time-mean quantities arising from initial conditions. Since sponge layers alone are an inadequate remedy, in PW's experience, we resort to a much deeper and wider domain, as in the study by SP, but with radiation conditions at both the upper and lateral boundaries.

A set of experiments based on the idealized initial environment and topography used by PW are described in section 2. The topic of section 3 is the momentum and energy budget for the developing and steady high drag state. The discussion in section 4 attempts to update the conceptual model of the high drag state and its development.

2. Experiments

Since we are assuming uniform wind and stability, incompressibility, and no background rotation, the response to a ridge in the topography is determined entirely by a Froude number, except for nonhydrostatic effects. Following PW, we define

$$\mathrm{Fr} \equiv Nh_0/u_0, \tag{1}$$

where h_0 is the maximum height of the mountain, u_0 is the undisturbed wind speed, and N is the undisturbed buoyancy frequency. Since Fr is the mountain height normalized by the scale of (hydrostatic) stationary waves,

$$h_g \equiv u_0/N, \tag{2}$$

it is a measure of the nonlinearity of the simplified system. Here we are interested only in cases with Fr of order unity or larger.

To neglect background rotation is to assume large Rossby number: $u_0/(fl_0) \gg 1$, where l_0 is the horizontal scale of the mountain and f is the Coriolis parameter.

[1] Laprise and Peltier (1989b) use Long's solution as their initial state in order to highlight modes of instability previously analyzed for that flow. This is not at all the limiting case of gradual start-ups from rest. The latter involve an extended period with *large* nondimensional mountain height, when Long's solution is meaningless. In the context of upstream influence, there is little point in comparing solutions like Laprise and Peltier's with those obtained using initialization from rest: permanent upstream alteration is insignificant in the part of parameter space where Long's solution applies (up to and just beyond the point of overturning stationary waves), regardless of the start-up procedure.

When Fr is of order unity or larger (the nonlinear regime), the disturbance is essentially hydrostatic over mountains with small aspect ratio, $h_0/l_0 \ll 1$. We are interested in the combined limits of small aspect ratio and large Rossby number. In this case, the only relevance of l_0 is in determining the advective time unit,

$$\tau_a \equiv l_0/u_0, \tag{3}$$

by which transient phenomena are measured.

According to PW, the upstream response following an impulsive start-up consists of decelerated flow in a near-mountain disturbance and in a separate propagating disturbance launched by wave breaking. Wave breaking and its far-field manifestations are present when the Froude number is greater than about 3/4. Near Fr $\approx$ 3/2, stagnant fluid begins to appear on the windward slope of the mountain. Finally, for Fr > 2, a layer of this blocked fluid surges upstream, according to PW. We will refer to these parameter boundaries as the wave breaking, stagnation, and blocking thresholds, in that order. The purpose of this section is to reexamine each threshold with special attention to the amplitude and duration of the changes with which it is associated.

a. The numerical model

The numerical model integrates the incompressible, nonhydrostatic equations in two dimensions, in vorticity–streamfunction format. The terrain-following grid has similar resolution to PW's near the ground: $\Delta z \approx 0.2h_g$ and $\Delta x \approx 0.2l_0$. However, the vertical resolution is finer at higher levels because the grid is not stretched. The domain width in the standard experiments is $50l_0$. The upstream boundary is at $x = -30l_0$, with the mountain centered at $x = 0$. The size of the domain is similar to that used by Lilly and Klemp (1979) and SP, but the horizontal resolution is much coarser than in the latter study. We forego accurate representation of extremely small space scales and timescales in order to obtain extremely long-term solutions in a wide range of cases. The experiments will be carried out to a time of $100\tau_a$, where τ_a is defined by (3). This is at least twice as long as in previous studies.

The upper boundary is "opened" by imposing the numerical radiation condition devised by Klemp and Durran (1983) for upward propagating, linear, hydrostatic gravity waves [the implementation is discussed further by Garner (1986)]. Although the boundary condition is also appropriate at finite amplitude for stationary hydrostatic waves (e.g., Lilly and Klemp 1979), it can still allow reflections of nonlinear *transients*. To test its effectiveness in highly nonlinear cases, a couple of the large Fr experiments to be presented were rerun with a sponge layer added to the upper part of the domain. Solutions using the sponge by itself were noticeably altered, but the combination of radiation and extra upper-level damping recovered the results achieved with radiation alone. Without the radiation condition, a deeper domain is required. Further control of reflections is achieved by locating the upper boundary at levels $z = (2n + 1/4)\pi h_g$, with n an integer. These are levels of relatively small vertical displacement, where advection and transient waves are treated most accurately by the boundary condition. We will use $n = 3$ when Fr ≤ 2 and $n = 4$, 5, or 6 when Fr > 2 (to keep the domain much deeper than h_0).[2]

The best results at the lateral boundaries are obtained by applying the standard wave advection condition (Orlanski 1976; Raymond and Kuo 1984) to the horizontal velocity u. The u profile may then be adjusted to maintain the initial horizontal mass flux, but this has little effect on the solutions if the domain is deep compared to the scale of internal waves. The lateral boundary scheme can become unstable if the temperature and momentum are extrapolated in the same way. Therefore, we assume zero normal gradient of the perturbation potential temperature (defined at doubly staggered points relative to the streamfunction and vorticity) in forming the normal component of temperature flux at inflow boundaries. Tests with an additional upstream sponge yielded essentially the same results as without, except that the sponge controls domain-averaged temperature trends otherwise present at large Fr. The extrawide domain provides room for dissipation and vertical dispersion of spurious reflections and more uncorrupted time for initialization.

Diffusion is applied explicitly to the vorticity, with a condition of zero eddy momentum flux, $\partial u/\partial z = 0$, at $z = h$ (lower boundary) and $z = H$ (upper boundary). Additional mixing (scale-sensitive diffusion) of temperature and vorticity is turned on whenever and wherever the local static stability falls below 10% of the ambient value. This scheme is certainly not as sophisticated as parameterizations based on the local Richardson number (e.g., SP). However, one may fairly conclude from previous modeling that the details of the convective adjustment scheme are not crucial for representing transience—including far-field transience—on timescales longer than the buoyancy period. The model diffusivity in overturning regions is limited to 10 times the background value. Heat is not diffused outside the regions of convection.

We adopt PW's choice of a Gaussian mountain profile, $h(x) = h_0 \exp(-x^2/l_0^2)$, and impulsive start-up of the wind. The choice for mountain aspect ratio is $h_0/l_0 = 0.05$. This keeps the flow essentially hydrostatic except in regions of convection. Convection starts at the steepening levels over the mountain, $z \approx (2n + 3/2)\pi h_g$ near $x = 0$, and extends downstream from there. Steepening levels are where u is a minimum in the linear

[2] With increasing Fr, it is increasingly difficult to keep the model depth large compared to the mountain height while resolving the waves adequately in the vertical. There is enough continuity in the present solutions to believe in their accuracy up to about Fr = 6.

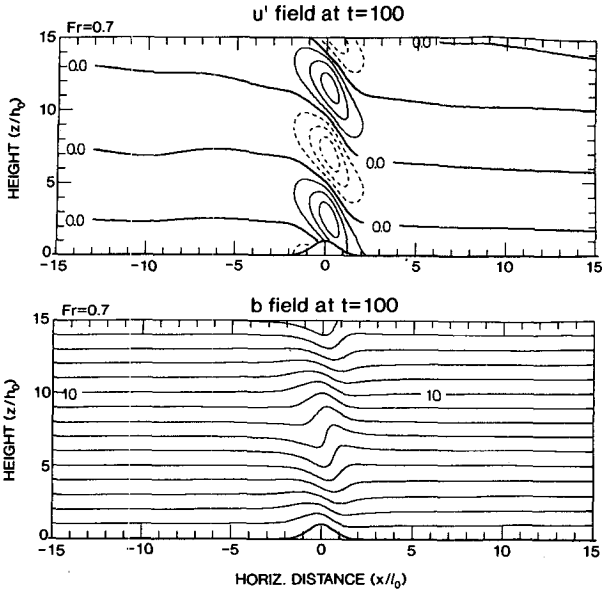

FIG. 1. Perturbation horizontal velocity (top) and total potential buoyancy (bottom) at time $t = 100\tau_a$ for the case Fr = 0.70, where $\mathrm{Fr} = Nh_0/u_0$. The horizontal and vertical axes are scaled by the mountain half-width l_0 and height h_0, respectively. Contour intervals: $\delta u = 0.1u_0$ and $\delta b = 1.0N^2h_0$.

stationary wave pattern. The internal hydraulic jump at the end of the shooting flow is also convective.

b. *Transient and time-mean behavior near the wave breaking threshold*

We equate wave breaking with the development of convective *turbulence* in the form of small wiggles in the isentropic contours. At the ground, turbulence is identified as the sudden appearance of drastically smaller space and time scales than in laminar solutions. These definitions are more practical than theoretical. A normal-mode analysis of Long's solution made by Laprise and Peltier (1989a) indicates that low-level wave breaking involves a type of resonant shear instability along with convective instability. With its slower growth rate and greater depth, the shear instability by itself may not generate the small time and space scales that would be recognizable as turbulence, especially in a diffusive model. There will be more to say later about the possible role of shear instability.

The model diffusivity is calibrated to provide marginal control of grid noise in nonbreaking solutions. At that setting, wave breaking first occurs at Fr = 0.76. This is some 10% smaller than the theoretical prediction[3] but consistent with previous results from time-dependent models. The turbulence in the solution with Fr = 0.76 occurs intermittently. Turbulent conditions become permanent for Fr = 0.77, in which case a shooting flow and high drag conditions develop. Thus, a small technical distinction (which we will not emphasize) may be made between the model's wave breaking and high drag thresholds. These thresholds are slightly sensitive to the diffusive flux condition at the lower boundary, as well as the diffusivity coefficient. An alternative condition of zero eddy vorticity flux ($\partial^2 u/\partial z^2 = 0$ instead of $\partial u/\partial z = 0$) reduces the breaking threshold by about 5%.

The solutions shown in Figs. 1 and 2 are for Fr = 0.70 and 0.80, respectively, at $t = 100\tau_a$. The first case has remained laminar for the duration of the experiment, and the flow shown is essentially Long's (1955) solution, with far-field conditions only minutely altered. In the other experiment, a distinctive high drag flow has developed. The wave breaking and low-level mixing begin at $t \approx 12\tau_a$. The mixed region starts out near $z = 5h_0$ over the mountain (the linear overturning height is 5.9 mountain units), whence it grows downstream, abreast with the shooting flow on the boundary. These structures terminate at an internal hydraulic jump, seen near $x = 8l_0$ in the figure. The bulk of the turbulence shifts from the mountain to the vicinity of the jump. These downstream developments are well known from previous studies.

In contrast to the drastic developments in the lee, the upstream disturbances in the two solutions are comparable. Conditions at higher levels are also comparable, although there is occasional overturning at the second steepening level in the second solution. The streamlines over the mountain are adjusted to critical

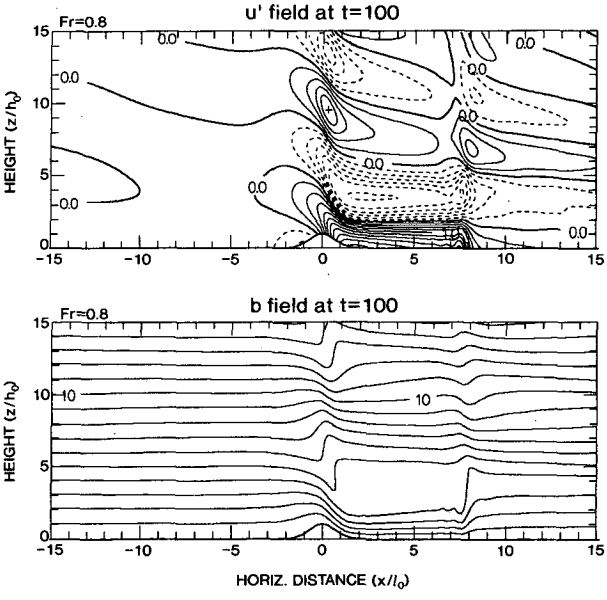

FIG. 2. As in Fig. 1 but for the case Fr = 0.80.

[3] The result for a bell-shaped mountain is Fr = 0.85 (Miles and Huppert 1969; Lilly and Klemp 1979).

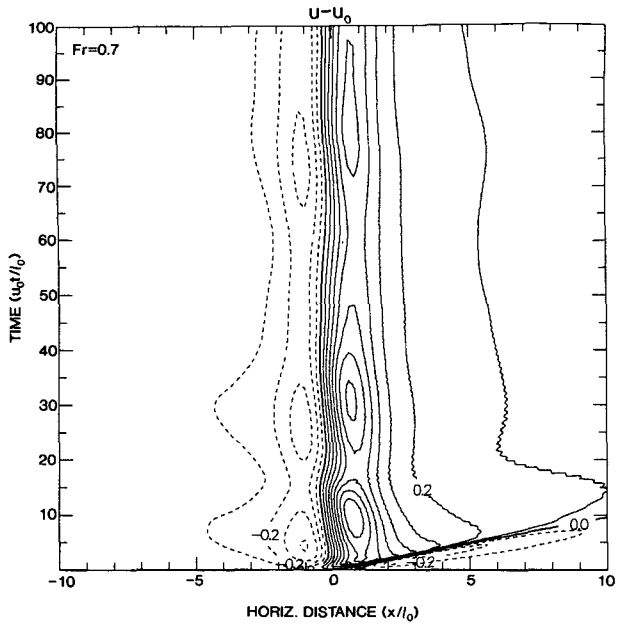

FIG. 3. Horizontal velocity perturbation at the ground as a function of time and distance from the mountain for the case Fr = 0.70. Contour interval: $\delta u = 0.1u_0$.

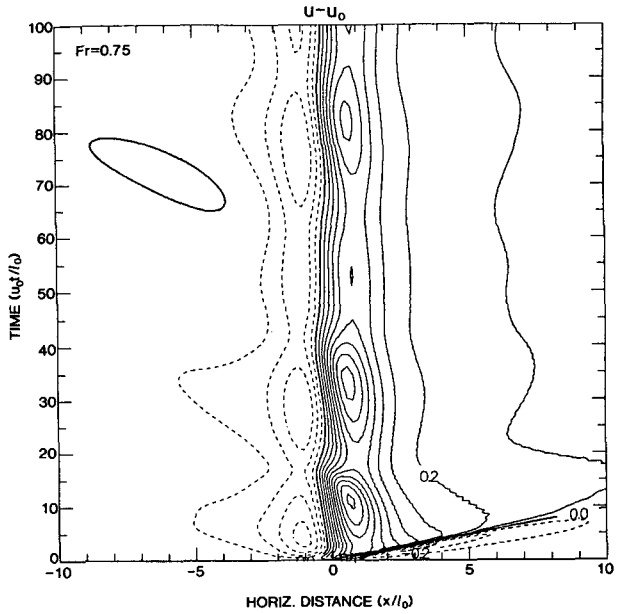

FIG. 4. As in Fig. 3 but for the case Fr = 0.75.

steepness by the combination of explicit and parameterized convection. As we will see in section 3, the total drag differs by a factor of about 3 between the laminar and breaking solutions. It is clear already that most of the difference is due to the shooting flow on the downslope.

The transition to wave breaking in time and with respect to Froude number can be studied in Figs. 3, 4, and 5. These are time–distance diagrams of horizontal velocity anomaly, $u' = u - u_0$, measured at the ground for the three cases Fr = 0.70, 0.75, and 0.80. The convective adjustment is turned off for all three experiments in order to make intercomparison as unambiguous as possible. This is the reason for the intense turbulence and grid noise in the third experiment (Fig. 5). The appearance of turbulence at the ground generally follows the onset of wave breaking in the interior by one or two time units.

There is persistent, quasi-periodic transience near the mountain on both sides of the wave breaking threshold. The timing (phase) of the transience changes only slightly across the threshold. However, there is a dramatic increase in the upstream penetration of the quasi-periodic signal. Unlike the long-term *mean* upstream value, which changes only slightly from $-0.4u_0$ to $-0.5u_0$, the transience becomes significantly stronger, increasing to about $0.4u_0$ from about $0.2u_0$ in total variation. Farther upstream at $x = -20l_0$, the maximum deceleration jumps from zero to about $-0.1u_0$. In PW's results, the far-upstream wind perturbation changes from zero to about $-0.2u_0$ across the breaking threshold. Their integrations are not long enough to extract any time-mean quantities for comparison. However, the present results suggest that the jump in upstream conditions across the breaking threshold belongs mostly to a *temporary* disturbance caused by the wave breaking.

There are two kinds of surface convergence zones in the lee of the mountain. The sharper one in Figs. 3–5

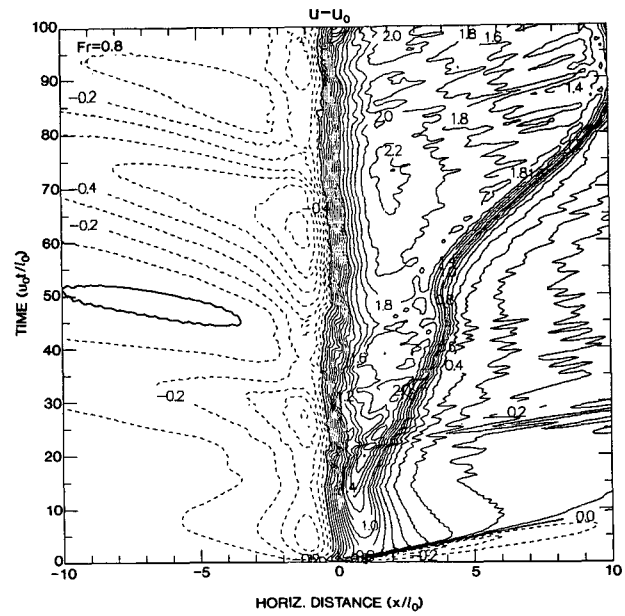

FIG. 5. As in Fig. 3 but for the case Fr = 0.80.

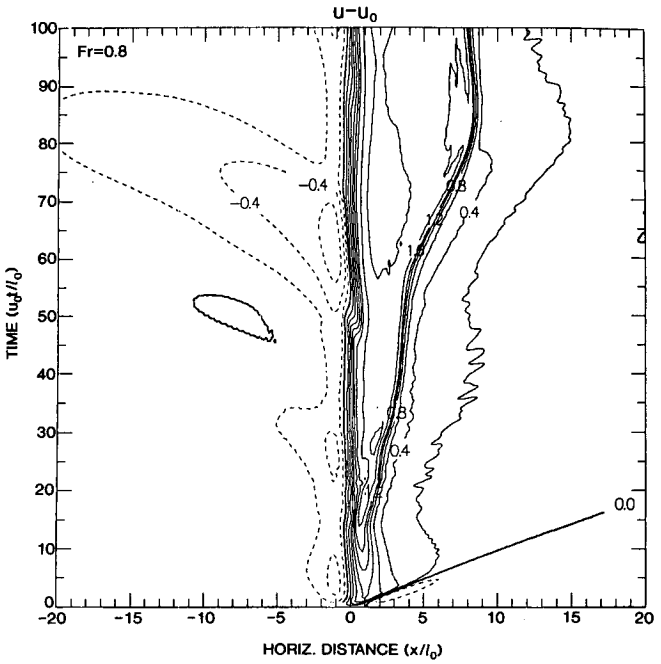

FIG. 6. Horizontal velocity perturbation at the ground as a function of time and distance from the mountain for the case Fr = 0.8. The experiment is the same as for Fig. 5 except that convective adjustment is activated. Contour interval: $\delta u = 0.2u_0$.

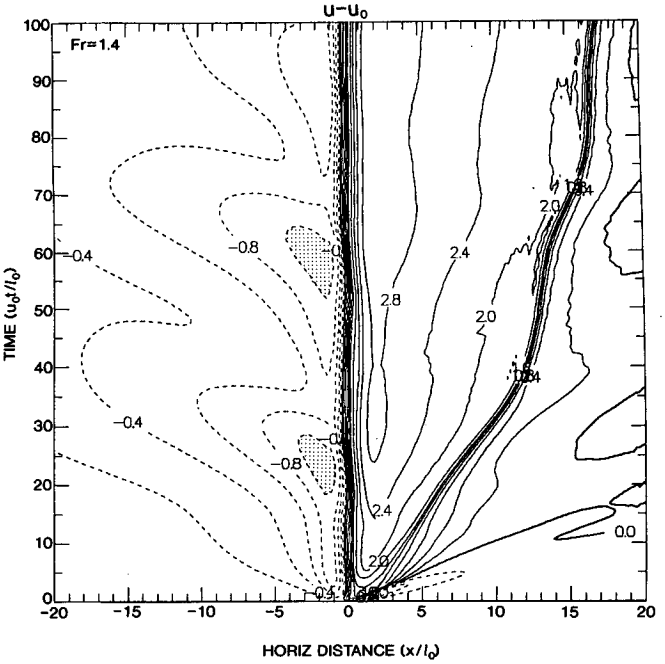

FIG. 7. As in Fig. 6 but for the case Fr = 1.4. Stippling indicates a region of stagnated or reversed flow.

is a response to the potentially warm strip located atop the ridge in the initial state. The other forms only in the breaking solution, at the base of the hydraulic jump. This is the chinook front (e.g., Scinocca and Peltier 1989). Compared to the warm front, which follows the basic flow at $dx/dt \approx u_0$ (for a nondimensional $x-t$ slope of unity), the chinook front moves slowly and spasmodically. In the present solution, it becomes stationary near $x = 4l_0$ for a short time beginning at $t = 45\tau_a$.[4] The halting movement of the hydraulic jump and the persistence of the near-mountain transience, especially in solutions below the breaking threshold, are unexpected. We return to this issue at the end of the section.

c. *Transient and time-mean behavior near the stagnation threshold*

The upstream disturbance first develops a region of stagnation for Fr between 1.3 and 1.4. This is smaller than PW's stagnation threshold of 1.5. Other changes across this parameter boundary can be seen by comparing Figs. 6, 7, and 8, which are time–distance plots of u' at the surface for Fr = 0.8, 1.4, and 2.0, respectively. The convective adjustment routine is activated for all of these solutions, which accounts for any dif-

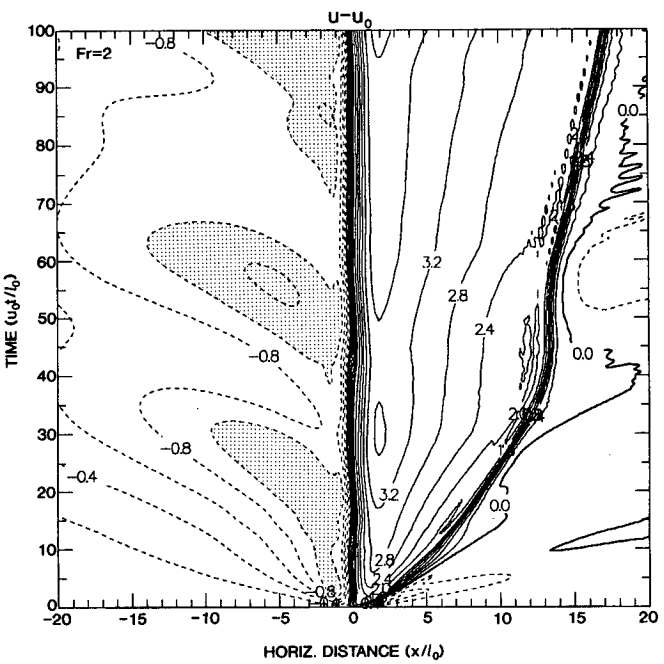

FIG. 8. As in Fig. 6 but for the case Fr = 2.0. Stippling indicates a region of stagnated or reversed flow.

[4] At early times, the flow near the warm front resembles that associated with the more slowly developing chinook front. The downslope convergence feature in Peltier and Clark's (1979) Figs. 7 and 8, which Laprise and Peltier (1989b) identify as the chinook front, is probably the start-up warm front instead. The development of a chinook front appears to require wave breaking.

ferences in data between Figs. 5 and 6. The main differences among the three solutions are 1) the time of the initial wave breaking, 2) the time-mean upstream deceleration, and 3) the speed of the hydraulic jump.

In the case Fr = 1.4, just past the stagnation threshold, there is wave breaking by $t = 10\tau_a$ and stagnant fluid on the windward slope by $t = 17\tau_a$ (recall that wave breaking is considered to begin with the development of small wiggles in the isentropic contours). In the case Fr = 2.0, stagnation occurs first, at around $t = 2\tau_a$, followed by wave breaking approximately one unit later. This last result shows that *wave breaking turbulence is not necessary for upstream stagnation.* For Fr $\geq$ 1.4, the hydraulic jump develops rapidly enough to involve air from the start-up warm strip: note that the usual surface convergence along $x = u_0 t$ is missing or weak in Figs. 7 and 8. A vertical cross section from the Fr = 2 solution is shown in Fig. 9. The strongest turbulence has shifted to the vicinity of the hydraulic jump, which has become an isolated source of quasi-stationary gravity waves.

The difference between the maxima and minima of u_s' (the anomaly at the surface) is about $0.4u_0$ in all three cases shown in Figs. 6–8. The onset of blocking as Fr increases is, therefore, mainly due to the smooth intensification of a *background* disturbance, that is, a time-mean upstream alteration. The time-averaged value of u_s' at $x = -20l_0$, which is a measure of the background disturbance, intensifies smoothly from $-0.1u_0$ when Fr = 0.8 to $-0.6u_0$ when Fr = 2.0. It has been noted that the wave breaking process is not necessarily heralded by turbulence. However, as long as there is no sharp transition in time-averaged conditions *near* the overturning threshold, one is obliged to rule out a significant wave breaking contribution to the background disturbance.

A further demonstration that the upstream background conditions do not depend on wave-induced instability is obtained by adjusting the terrain shape. Lilly and Klemp (1979) observe that, by broadening the lee slope of the mountain, the stationary wave train can be "unsteepened" at the levels $z = (2n + 1/2)\pi h_g$ without weakening the upstream deceleration at the levels $z = 2n\pi h_g$ (in fact, steady-state linear theory predicts an infinite upstream response in the limiting case of a "ramp" profile). Such a mountain should yield a strong initial surge with suppressed wave breaking transience. That result is clear in Fig. 10, which shows vertical cross sections for the lee-broadened mountain experiment with Fr = 2 (convective adjustment is turned off to emphasize the weak production of turbulence in this case). Although the flow is only at the verge of critical steepening at the time shown, the upstream columnar disturbance is well established. Moreover, the wave steepening occurs far enough downstream to have minimal impact on the upstream disturbance at early times. The time–distance plot of u_s' for this experiment is shown in Fig. 11. It clearly connects the background disturbance to the initial surge.

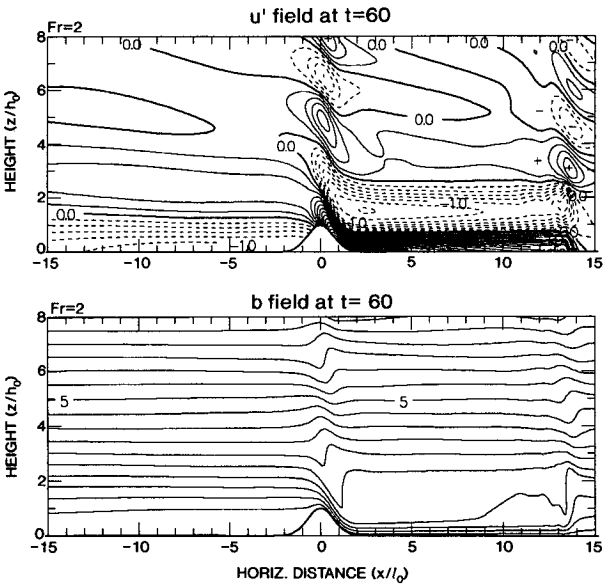

FIG. 9. Perturbation horizontal velocity (top) and total potential buoyancy (bottom) at $t = 60\tau_a$ in the case Fr = 2.0. Contour intervals: $\delta u = 0.2u_0$ and $\delta b = 0.5N^2h$.

d. *Transient and time-mean behavior near the blocking threshold*

The final threshold identified by PW involves what could be called a "blocking surge." The present solutions do not show any abrupt change in *time-mean* conditions corresponding to such a threshold or surge. As Fr increases, the time-mean size of the region with $u_s' \leq -1$ increases gradually and the time variability of this blocked area decreases. Figure 12 shows $u_s'(x, t)$ for the case Fr = 3.0. (The size of the equilibrated shooting region begins to *decrease* for Fr beyond 2.0. The reason for this behavior is not known.) It is near this value of Fr = 3.0 that the blocked region extends permanently to the upstream boundary ($x = -30l_0$). Closer to the mountain at $x = -20l_0$, the time mean of u_s changes sign at a somewhat smaller value. The limit on the size of the time-mean blocked area is probably imposed by frictional damping of upstream-propagating signals, as there are no inviscid, stationary disturbances with finite horizontal scales over flat terrain. It is reasonable to infer a Froude number threshold somewhere between 2.5 and 3.0, depending mainly on the model dissipation, at which the background disturbance becomes fully blocked. Recall that PW locate their blocking threshold at Fr $\approx$ 2.0. Evidently, we have refined this parameter boundary by filtering the contribution from the persistent transience.

Beyond Fr = 2.5, there is good evidence of the "orographic adjustment" mentioned by PW. In this process,

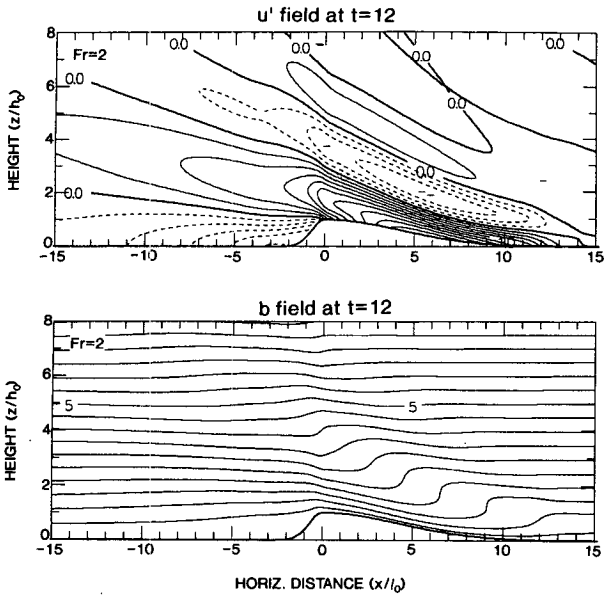

FIG. 10. As in Fig. 9 but for the lee-broadened mountain with half-widths l_0 (upstream) and $6l_0$ (downstream).

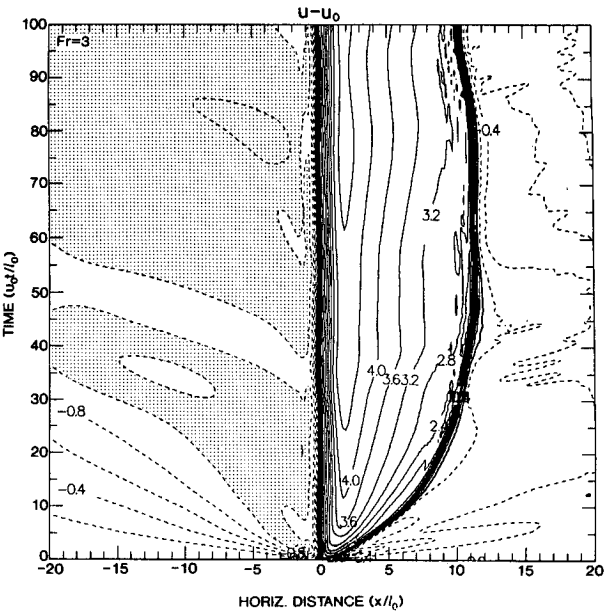

FIG. 12. Horizontal velocity perturbation at the ground as a function of time and distance from the mountain for the case Fr = 3.0. Stippling indicates a region of stagnated or reversed flow. Contour interval: $\delta u = 0.2u_0$.

a layer of fluid becomes permanently blocked upstream with sufficient depth to keep the effective height of the mountain (as measured above the stagnant layer) at the marginal value for permanent blocking. Shown in Fig. 13 are time-averaged vertical profiles of $u'(z)$ at the upstream point $x = -10l_0$ for Fr ranging from 1 to 5. Following PW's argument, the depth d of the blocked layer should vary according to $d/h_0 = 1 - \mathrm{Fr}_b/\mathrm{Fr}$, where Fr_b refers to the permanent blocking threshold. If we take Fr_b to be 2.5, the data seem to support the hypothesis of orographic adjustment.

Shown in Fig. 14 are profiles of time-averaged total streamfunction $\psi(z)$ measured in the downstream shooting region of the numerical solutions for a range of Froude numbers. The mass flux of the hydraulic layer, say ψ_h, is the value of ψ at its local maximum, since the fluid immediately above is overturning. For $\mathrm{Fr} < \mathrm{Fr}_b$, the mass flux increases with Fr in qualitative agreement with the model of Smith (1985). In fact, the hydraulic mass flux at the blocking threshold, say ψ_{hb}, is well approximated by Smith's absolute maximum, $(3\pi/2)u_0h_g$ (numerically about 4.7). For larger Fr, the nondimensional flux is a nearly linear function of Fr. This is consistent with orographic adjustment, which

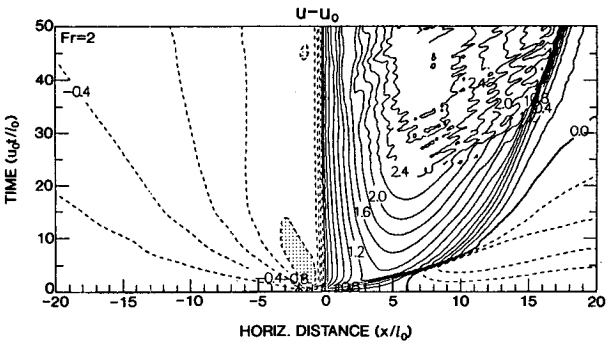

FIG. 11. Horizontal velocity perturbation at the ground as a function of time and distance from the summit of the lee-broadened mountain with Fr = 2.0. The convective adjustment is deactivated. Contour interval: $\delta u = 0.2u_0$.

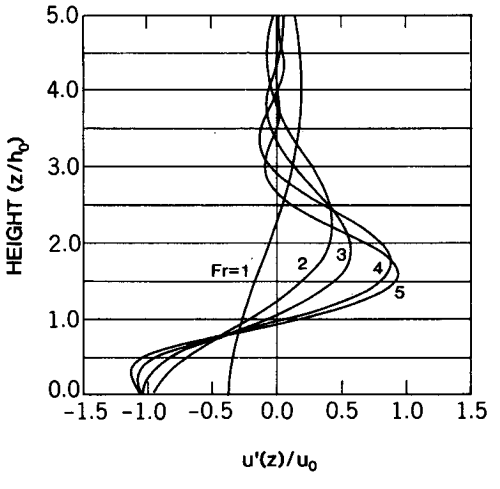

FIG. 13. Vertical profiles of time-mean horizontal velocity at $x = -10l_0$ for Fr ranging from 1 to 5. Vertical unit is the mountain height h_0.

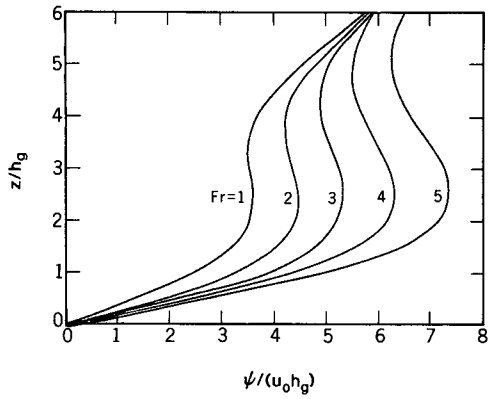

FIG. 14. Vertical profiles of time-averaged streamfunction at $x = 4l_0$ for Fr ranging from 1 to 5. Streamfunction and height are normalized by u_0h_g and h_g, respectively.

implies that $\psi_h = \psi_{hb} + \mathrm{Fr} - \mathrm{Fr}_b$. Smith's model grossly underestimates the maximum possible height of the mountain for unblocked high drag flows. We return to that problem in section 4.

e. *Persistent transience*

All solutions above Fr $\approx$ 0.5 show persistent quasi-periodic transience upstream, usually with synchronized downstream effects. This variability has a characteristic timescale ranging from $25\tau_a$ to $35\tau_a$. There is an indication of similar low-frequency behavior in PW's solutions: in their Figs. 4 and 5, a lull can be seen in the upstream surface wind anomaly during the period $t = 9\tau_a$ to $11\tau_a$. The oscillation is clearly different from the downstream pulses discovered by Scinocca and Peltier (1989) but is probably the same thing as the "interesting transience," which the same authors mention in passing remarks about the upstream disturbance.[5]

Each episode of enhanced upstream deceleration in the low-frequency oscillation begins with the collapse of steepened isentropes at the lowest steepening level over the mountain (Fig. 2 happens to show a time of maximum wave steepness). The collapse is turbulent in the breaking solutions. The steepened pattern is reestablished during the episodes of upstream maxima in u_s', when the upstream disturbance is weakest. This is especially clear in the nonbreaking solutions: for instance, in Fig. 4 at $t \approx 50\tau_a$ and $95\tau_a$. In breaking solutions with Fr < 2 (cf. Figs. 6–8), the oscillation is clearly synchronized with the downstream surges of the internal hydraulic jump.

Further experiments reveal some sensitivity, in both the amplitude and the frequency of the transience, to the placement of the upper boundary (there is no comparable sensitivity to the lateral boundary location). However, we find that the period of the oscillation does not depend linearly on the distance to the upper boundary and that the amplitude is not very sensitive to the introduction of an upper sponge. For these reasons, the transience is not believed to be a numerical artifact. In special experiments in which linear damping is applied at the first steepening level, the oscillation can be strongly suppressed after the first cycle, even when the long-term mean is essentially unaffected. Only the first cycle appears to be sensitive (in amplitude) to the way in which the large-scale flow is started.

In Fig. 15, the vertical structure of the low-frequency oscillation is shown in time–height format. The average of u between $x = 0$ and $x = 1.0l_0$ is plotted as a departure from the long-term mean for the laminar case Fr = 0.75. The vertical axis is the model coordinate ζ, which is not quite the same as height [ζ is a linear mapping from $(0, H)$ to (h, H)]. A more useful vertical reference is available in the pattern of stationary waves along the axis $t = 0$, where the long-term mean vertical structure appears with reversed sign. Note that the transient pattern has approximately the same wavelength as the stationary wave train but is phase shifted by a quarter wavelength. The buoyancy (not shown) also has this phase shift, relative to the long-term mean. The vertical phase shift is consistent with a quarter-wave-

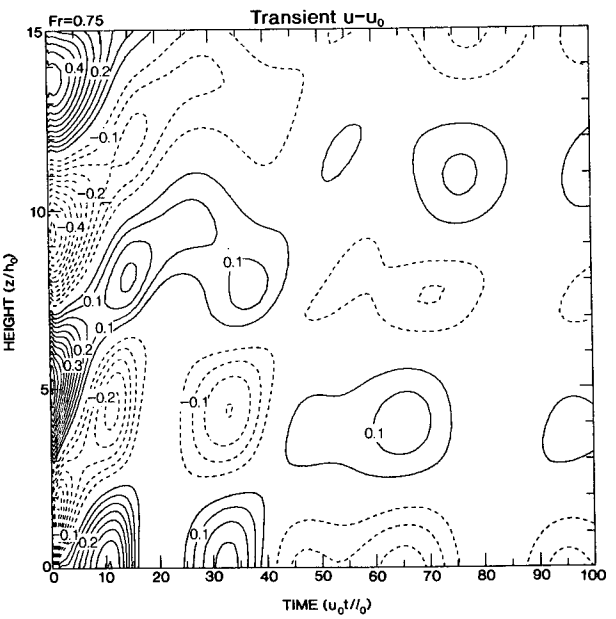

FIG. 15. Transient part of horizontal velocity averaged between $x = 0$ and $x = l_0$ as a function of time and ζ (the terrain-following vertical coordinate) for the case Fr = 0.75. The vertical coordinate is normalized by h_0. Contour interval: $\delta u = 0.05u_0$, zero suppressed.

[5] Scinocca and Peltier's downstream pulses have a timescale of less than τ_a. The streaks that appear in the shooting region late in the experiment shown in Fig. 5 are similar in some respects to their pulses, but are much weaker.

length horizontal (specifically downstream) displacement over sinusoidal topography.

The time–height tilt suggesting vertical propagation above the first steepening level in Fig. 15 is similar to the tilt of the edge of the start-up region: both follow the group speed of stationary hydrostatic modes with horizontal wavelength comparable to the mountain width, $t/\tau_a \approx \pi^{-1} z/h_g$. A time–distance plot of the transient part (departure from the overall time mean) of u_s' is shown in Fig. 16. As might be expected from the group speeds, the horizontal scale of the transience is similar to that of the stationary disturbance (the mountain scale). However, there is obviously horizontal as well as vertical propagation here. The apparent source of the upstream-propagating pulses is between $x = l_0$ and $x = 2l_0$. Upstream of $x = 0$, where steepening occurs at a higher level and is less severe, propagation becomes faster and the pattern weaker. There is no evidence of *downstream* signal propagation in Fig. 16, except for the start-up warm front. Downstream signals are mainly confined to the shooting flow, which is much shallower than the layer used for the vertical averaging.

The unexpected low-frequency variability undoubtedly results from *internal* absorption, reflection, and reradiation of momentum fluxes, focused mainly at the first steepening level but possibly involving higher levels. The vertical phase of the disturbance in Fig. 15 is fairly fixed over time, but the time variation of the amplitude (presumably due to wave *groups*) suggests *partially ducted waves.* Thus, there is considerable energy reflection in the layer between the ground and the first steepening level (near $z = 5h_0$) but free group propagation from there upward. Bacmeister and Schoeberl (1989) are able to demonstrate internal reflection with comparatively little ambiguity because of the greater distance from the breaking level to the surface. Breaking occurs at high levels in their solutions because of a background vertical density gradient. The period of the present oscillation is less likely to be determined by linear dynamics. The discrepancy between the lateral and vertical energy propagation speeds already implies nonlinear conditions over a wide region.

The "deep resonant modes" found by Laprise and Peltier (1989a, hereafter LP) also depend on the reflectivity of the medium at the top of the overturning layer. These linear modes (of Long's nonlinear solution) have a vertical wavelength close to that of the stationary wave pattern (cf. LP's Fig. 11), as do the present experimental modes. However, they do not clearly exhibit the surface maximum of kinetic energy that is seen in the experiments. Nor do they propagate relative to the mountain. These differences may be mostly attributable to the linearity of LP's analysis. A linear analysis also cannot incorporate changes in the reflectivity that could cause an oscillation in the amplitude of the trapped mode. In speculating about the nonlinear evolution of their unstable modes, LP do not consider the possibility of periodic behavior. However, they do show that the shear modes expend energy working against buoyancy, and this is consistent with a mechanism for restoring the vertical thermal gradient and propagation medium. Laprise and Peltier point out that *neutral* shear modes are important because they can be forced at the lower boundary. Indeed, we observe persistent transience even in experiments below the breaking threshold, where the linearized shear modes are stable.

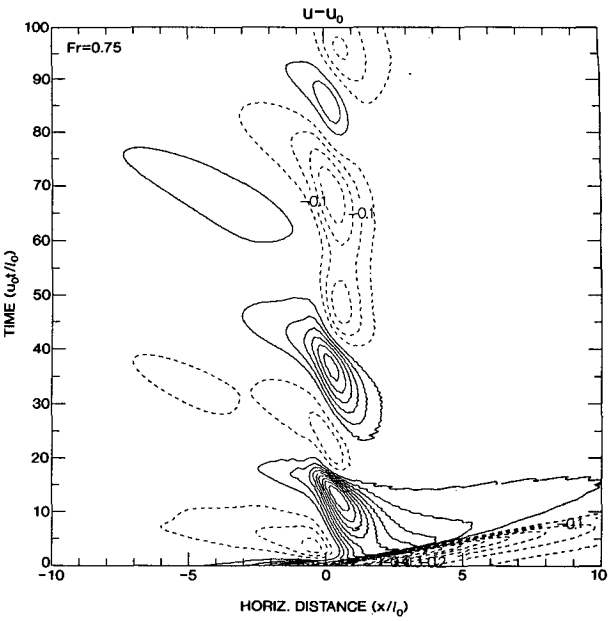

FIG. 16. Transient part of horizontal velocity at the ground as a function of time and distance from mountain for the case Fr = 0.75. The horizontal coordinate is normalized by l_0. Contour interval: $\delta u = 0.05u_0$, zero suppressed.

3. Momentum and energy

Wave drag parameterization schemes for large-scale models normally obtain their estimate of total drag from a model of linear, hydrostatic, stationary gravity waves. During "severe wind" conditions, such estimates fall well short of the drag known from mesoscale simulations. To correct for high drag conditions, Shutts (1990) suggests changing smoothly to a nonlinear estimate like that of Smith (1985) as the high drag state becomes more probable. Pierrehumbert (1986), concentrating on the fluxes above the hydraulic layer, proposes a similar procedure based on marginal low-level wave saturation. Both of these alternatives yield a stress that is $O(\mathrm{Fr}^{-2})$ times the linear result for total drag. As we will see, that is still the wrong parameter dependence for the total drag in the nonlinear regime.

Since the drag in severe wind states is deposited in the layer beneath the first breaking level (Peltier and Clark 1983; Durran 1986), steady near-mountain con-

ditions in that layer require steady *horizontal* momentum fluxes and an ever-widening disturbance. Naturally, the momentum budget provides the best picture of how blocking and stagnation are connected to the mountain forcing. Scinocca and Peltier (1989) observe that low-frequency variability in the movement of the hydraulic jump, which we have related to steepening/unsteepening transience, is synchronized with plateaus in the wave drag time series. Here we are interested in the upstream imprint of these local saturation events, as SP refer to them. The perturbation energy budget will also be considered, partly because it helps to establish the analogy with hydraulic theory.

The momentum budget in the inviscid Boussinesq system is

$$\frac{\partial u}{\partial t} = -\nabla\cdot\mathbf{F}_u, \tag{4}$$

where $\mathrm{F}_u = u'\mathbf{V} + p'\hat{\mathbf{x}}$ (the perturbation momentum flux), $\mathbf{V} = u\hat{\mathbf{x}} + w\hat{\mathbf{z}}$, and p is the pressure divided by the constant density. The prime denotes a departure from the state with constant velocity and stratification. The unit vectors have been written as $\hat{\mathbf{x}}$ and $\hat{\mathbf{z}}$. Integrating (4) over a region $\mathscr{R}$ yields

$$\frac{\partial}{\partial t}\int\int_{\mathscr{R}} u'dA = \int_{\partial\mathscr{R}} F_{un}ds, \tag{5}$$

where the integral along the perimeter $\partial\mathscr{R}$ is in the clockwise tangential (s) direction and $F_{un} = u'\partial\psi/\partial s + p'\partial z/\partial s$, the inward normal flux component.

Since $\partial\psi/\partial s = 0$ on the solid boundary, the total momentum sink, assuming zero flux at infinity, is

$$\frac{\partial\langle -u'\rangle}{\partial t} = \int_{\zeta=0} p'dz = D, \tag{6}$$

where the angle brackets denote a full volume integral and D stands for total drag. The integral is taken along $z = h(x)$. In linear, hydrostatic flow over a Gaussian ridge, we have $D = 0.9$ Fr in units of $u_0^2h_0$. At marginal saturation (order-unity Froude number), both u' and w change from $\mathrm{O}(Nh_0)$ to $\mathrm{O}(u_0)$, and the scaling for the vertical flux accordingly changes by a factor of $1/\mathrm{Fr}^2$ (e.g., Lindzen 1981; Pierrehumbert 1986).

We also consider the quantity $E = \frac{1}{2}(|\mathbf{V}'|^2 + b'^2/N^2)$, where N^2 is a constant (we will use the undisturbed value of the static stability) and b is the usual potential buoyancy for the Boussinesq model. In the absence of dissipation, the energy E obeys

$$\frac{\partial E}{\partial t} = -\nabla\cdot\mathbf{F}_E, \tag{7}$$

where $\mathbf{F}_E = E\mathbf{V} + p'\mathbf{V}'$. The budget for E is informative if the environment has small variations of static stability [E satisfies (7) in any case]. Since $\mathbf{F}_E = (E + p')\mathbf{V} - u_0p'\hat{\mathbf{x}}$, a volume integral of (7) may be written

$$\frac{\partial}{\partial t}\int\int_{\mathscr{R}} EdA = \int_{\partial\mathscr{R}} F_{En}ds, \tag{8}$$

where $F_{En} = (E + p')(\partial\psi/\partial s) + u_0p'(\partial z/\partial s)$.

Integrated over the full atmosphere, the energy flux convergence is proportional to the drag. Thus,

$$\frac{\partial\langle E\rangle}{\partial t} = u_0D. \tag{9}$$

It follows from (6) and (9) that the *total* energy, $E_T \equiv E + u_0^2/2 + u_0u'$, obeys the simpler constraint,

$$\frac{\partial\langle E_T\rangle}{\partial t} = 0. \tag{10}$$

Since E_T has no external sources, it is more natural to describe disturbances in terms of E.

a. Local budgets

The values plotted in Fig. 17 are of the integrated flux of negative momentum across the model coordinate surfaces, $\zeta = 0$ and $\zeta = 5\pi h_g$, averaged in time between $t = 40\tau_a$ and $60\tau_a$. The flux across the higher surface, the residual flux, differs from the flux across

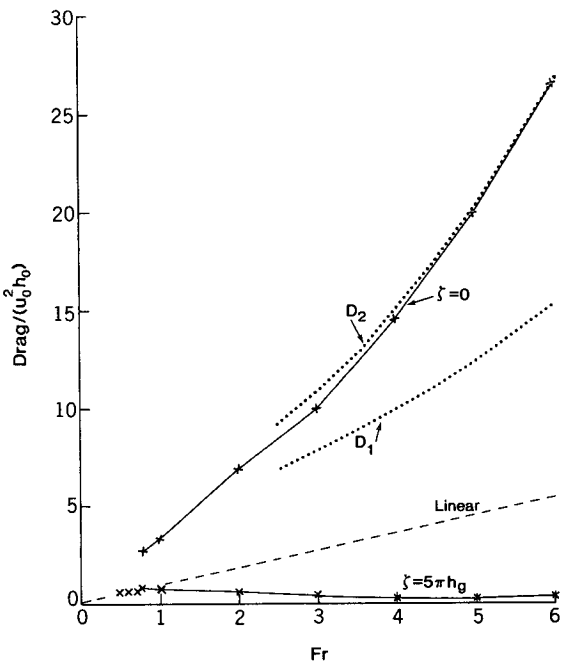

FIG. 17. Total vertical flux of negative momentum as a function of nondimensional mountain amplitude Fr according to a number of experiments and models. Mountain shape is Gaussian. Solid lines show the numerical model result at the ground ($\zeta = 0$) and in the residual wave train ($\zeta = 5\pi h_g$). Dashed line is the linear drag prediction $D = 0.9$Fr. Dotted lines show the nonlinear estimates D_1 and D_2 derived in section 4. Experimental values, indicated by ×, are averaged over a period of 20 advective time units (τ_a) centered at $t = 50\tau_a$. Vertical axis scaled by $u_0^2h_0$ (density understood).

$\zeta = 0$, the total drag, only in the high drag cases. The total drag jumps by a factor of about 3 at the wave breaking threshold. In Long's solution for flow over a bell-shaped mountain, the drag increases *smoothly* by the same factor between Fr $\approx$ 3/4 (the breaking threshold in initial value experiments) and Fr $\approx$ 2 (Lilly and Klemp (1979). Pierrehumbert (1986) computes the drag exerted by a Gaussian mountain up to Fr = 2 in experiments like the present ones. His results are slightly larger for the residual flux and slightly smaller for the total drag, especially for the larger values of Fr in his range.

The linear solution, shown by the dashed line in Fig. 17, is an acceptable estimate of drag in the nonbreaking solutions. Beyond the breaking threshold, the residual flux is in reasonable agreement with the saturation hypothesis, which implies inverse proportionality to Fr in the present units. This was previously established by Peltier and Clark (1983). On the other hand, the total flux at the ground increases with Fr. Smith's (1985) model drag has the saturation parameter dependence $D \sim \mathrm{Fr}^{-1}$ and therefore gives an even worse prediction of total flux than the linear model. In section 4, we will see whether an adjustment for upstream stagnation can bring Smith's formula more in line with the experiments.

Given finite signal speeds, only locally steady states can be established in a finite time. To examine the steady-state budgets, we choose a control volume over the mountain and compute time-averaged fluxes there during the second half of the experiments. The interval $-5l_0 < x < 5l_0$ is used for the momentum and $-2l_0 < x < 2l_0$ for the energy (the energy budget in the larger interval is strongly affected by dissipation). The top of the volume is put at $\zeta = 3\pi/2h_g$, the nominal upstream height of the hydraulic layer and the lowest overturning level. During the averaging period, the downstream measurements fall within the region of the shooting flow in the breaking cases. The pressure is diagnosed from the velocity data by spatially integrating the momentum equation in the form

$$\nabla p' = -\nabla E_K + \eta \nabla \psi - (\partial/\partial t)\mathbf{V} + b'\hat{\mathbf{z}} \quad (11)$$

from a point with $p' = 0$ at the upstream top corner. Here $E_K \equiv |\mathbf{V}|^2/2$ (the total kinetic energy), ψ is the streamfunction, and η is the vorticity.

As in section 2, we concentrate on the symmetric mountain with Fr = 2.0. The vertical and horizontal momentum flux profiles are shown in Fig. 18. The vertical component (Fig. 18b) has been computed as $F_{un}(ds/dx)$ so that the total flux across the surface is an integral with respect to x. The total flux across $\zeta = 0$ comes to about $7.6u_0^2h_0$, exceeding the linear estimate of total drag by a factor of 4. (This is somewhat larger than the result plotted in Fig. 17. The latter was obtained using a deeper domain with slightly less resolution. Also, the averaging periods are different.) The contribution from the leeward slope dominates, but the asymmetry here is smaller than at the breaking threshold.

The near-saturation flux out of the top of the volume represents only 6% of the budget. The drag is therefore balanced mainly by convergence of the horizontal momentum flux (Fig. 18a). The vertical integral of this flux,

$$\int_0^{H_0} (\mathbf{F}_u \cdot \hat{\mathbf{x}}) dz \equiv \hat{F}_{ux}, \quad (12)$$

is the so-called flow force (Benjamin 1968) perturbation. It is roughly equal and opposite on the upstream and downstream sides. The negative flux in the lee is mainly due to low hydrostatic pressure, which is enhanced by the cascading structure. At values of Fr

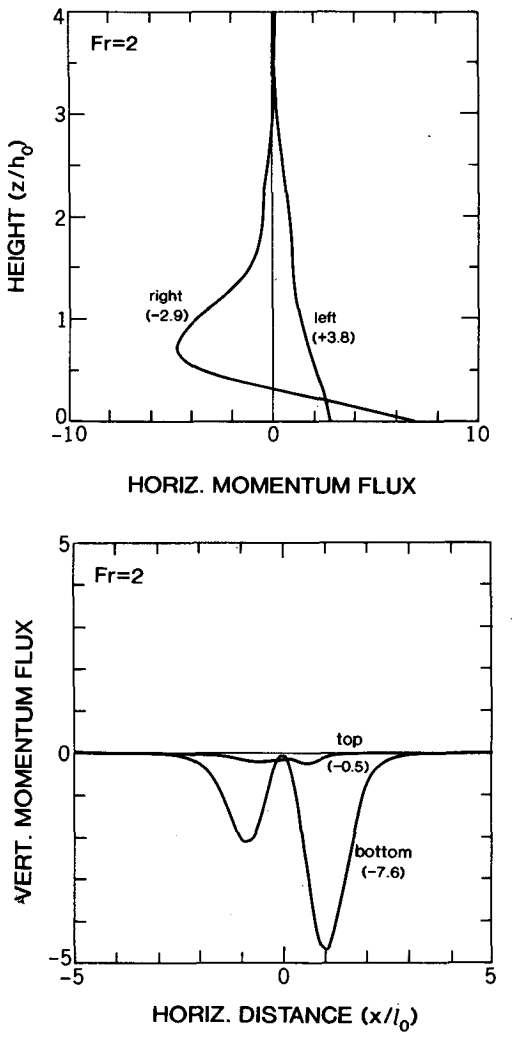

FIG. 18. Time-averaged horizontal (top) and vertical (bottom) components of momentum flux as a function of height or horizontal distance for the case Fr = 2. The four curves correspond to the four sides of the control volume described in text. Units are u_0^2 for F_{ux} and $u_0^2(h_0/l_0)$ for F_{uz}.

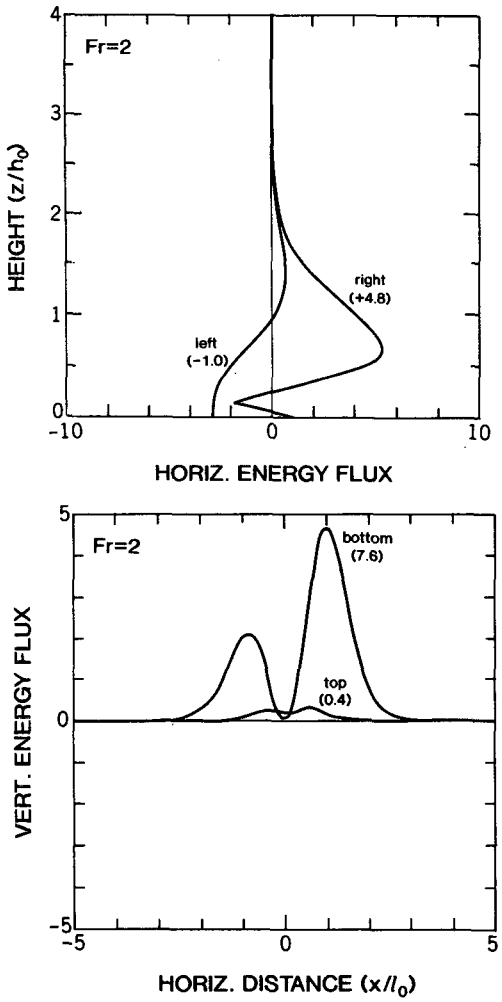

FIG. 19. Time-averaged horizontal (top) and vertical (bottom) components of perturbation energy flux for the case Fr = 2. Units are u_0^3 for F_{Ex} and $u_0^3(h_0/l_0)$ for F_{Ez}.

nearer the wave breaking threshold, this effect dominates. The flux diverges in the lowest two grid points. Elsewhere in the column, it is directed toward the mountain from both sides. Taking into account the flux out of the top of the volume, we compute a residual momentum *source* of about 5% due to dissipation and differencing error.

The energy flux profiles are shown in Fig. 19. At $\zeta = 0$, the vertical flux has the same horizontal profile as the drag [cf. (6)]. The total source of perturbation energy is the same as the momentum sink multiplied by u_0. About three-fourths of the energy is radiated laterally. The remainder is either dissipated (18%) or lost to the upper atmosphere (6%). The horizontal energy flux is divergent at all levels (Fig. 19a). It is generally directed upstream on the windward side and downstream on the leeward side. Since the fluxes in the lee are stronger than the windward fluxes, we infer that total energy E_T is transferred systematically across the mountain from points upstream to points downstream (the horizontal component of $\mathbf{F}_{ET} = \mathbf{F}_E + u_0\mathbf{F}_u + (u_0^3/2)\hat{\mathbf{x}}$ is positive).

The time–distance plot in Fig. 20 shows the vertically integrated horizontal momentum flux (flow force) as a function of x. Note that the background pattern is established during the first 5 time units or so. The transience is similar to that of the surface momentum (Fig. 8). It is fair to conclude that the wave breaking episodes at $t \approx 30\tau_a$ and $t \approx 60\tau_a$ (cf. Fig. 8) leave no significant permanent imprint on the upstream disturbance. The imprint is not clear downstream, where we see a negative trend in the horizontal flux. This trend is also present in the drag and dissipation (not shown). The trend in the flux is mainly due to the pressure anomaly, which naturally dominates the flow force at large Froude number. The implied intensification of the downstream horizontal pressure *gradient* corresponds to an acceleration of the overturning circulation at the top of the control volume.

The horizontal flux of perturbation energy is shown in Fig. 21. While the hydraulic jump does not block or dissipate much of the vertically integrated momentum, it is evidently a strong barrier to the energy flux. This evokes the classic picture of momentum-conserving shocks (e.g., Stoker 1957, section 10.6) and helps establish the analogy between the turbulent jumps in the stratified and true hydraulic systems. There is energy flux convergence everywhere in the lee, but especially

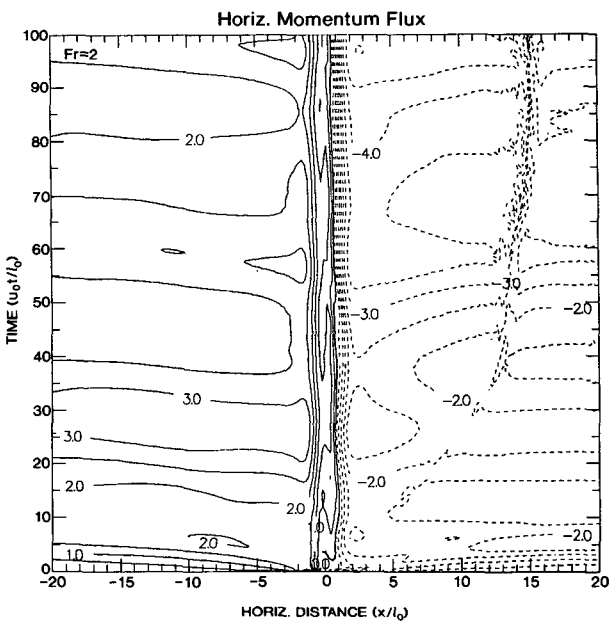

FIG. 20. Vertically integrated horizontal momentum flux (flow force) as a function of time and distance from mountain for the case Fr = 2. Vertical integral covers $\zeta = 0$ to $\zeta = (3\pi/2)h_g$. Contour interval: $\delta\hat{F}_{ux} = 0.5u_0^2h_0$.

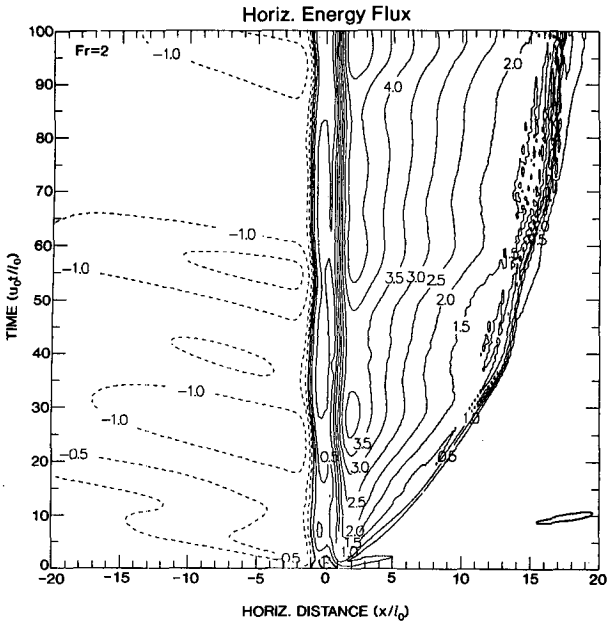

FIG. 21. Vertically integrated horizontal energy flux as a function of time and distance from mountain for the case Fr = 2. Integral covers the same vertical interval as for Fig. 20. Contour interval: $\delta\hat{F}_{Ex} = 0.5u_0^3h_0$, except the -0.25 contour is also drawn.

at the hydraulic jump. Since very little energy escapes vertically, most of the horizontal convergence must be balanced by dissipation. In particular, the hydraulic jump absorbs and destroys nearly all of the energy that survives the shooting flow. The extension of the shooting region requires increases in the horizontal flux near the mountain (the energy supply) to balance the dissipation. The supply increases in spurts that are synchronous with the wave breaking episodes and hydraulic surges. Upstream, the wave breaking transience produces factor of 2 increases in the flux, but these are known to be temporary.

Finally, we return to the laminar case Fr = 0.75. The quasi-periodic transience discussed in section 2 now appears in the time–distance plot of energy flux, Fig. 22. The bursts over the leeward slope (Fig. 22a) correspond to the upstream-propagating pulses in the surface wind (Fig. 16). Since energy advection is strictly downstream (positive), the sign of the energy flux is controlled by a comparatively strong pressure flux associated with a negative flow-relative group velocity. For ease of interpretation, the averaging interval for this calculation is extended to $z = 2\pi h_g$. Over this layer, there is zero net energy flux across vertical lines in the steady-state, linear solution. Figure 22b shows the net divergence of *vertical* energy flux within the layer. The pattern indicates that the transient energy originates over the downslope, where the flux is convergent. Much of the energy then escapes to higher levels before getting far upstream, as shown by the region of net divergence between $x = 0$ and $x = -l_0$. There is a similar transfer of drag across the mountain (not shown). The upstream transfer takes about 4 time units. This is the solution with the strongest nonturbulent transience. As Fr increases, the energy bursts eventually become turbulent and the energy reaches much farther upstream. The distinction between near mountain and far upstream (PW) seems almost meaningless in that case. The next subsection takes a closer look at signal speeds in the turbulent solutions.

b. *Signal speeds*

Energy in hydrostatic gravity waves travels horizontally at the same speed as the phase. Since the phase speed depends only on vertical structure, a horizontally localized disturbance may retain its shape for long times if the amplitude is concentrated in a small range of vertical scales. In the time–distance analyses of flow force and energy flux, Figs. 20 and 21, there is considerable coherence in the shape of both the initial surge and wave breaking surges. From the slope of the contours in the plots, we estimate a signal speed of about $-4u_0$ for both types of surge. This corresponds to a vertical wavelength 5 times that of the stationary modes. (Hence, it is consistent to neglect a vertical density variation with scale height greater than about

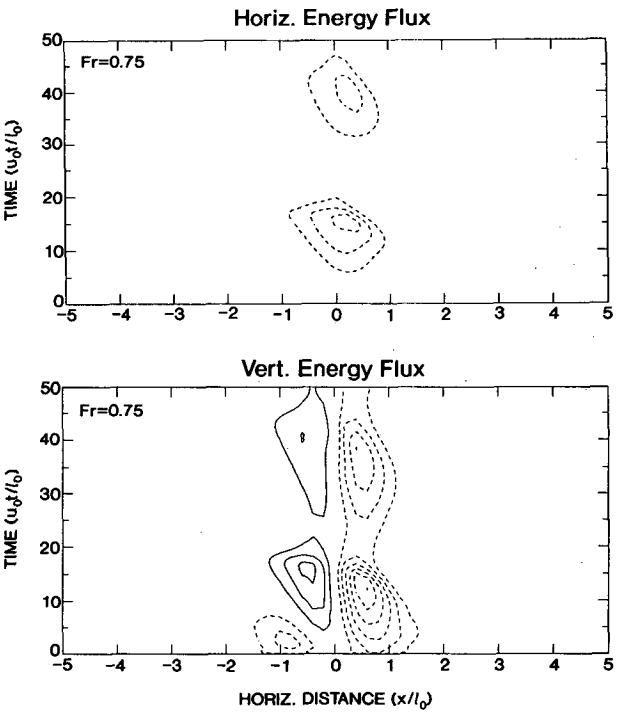

FIG. 22. Vertically integrated horizontal energy flux (top) and vertical flux divergence (bottom) as a function of time and distance from the mountain for the case Fr = 0.75. Integral covers $\zeta = 0$ to $\zeta = 2\pi h_g$. Contour interval: $\delta\hat{F}_{Ex} = 0.2u_0^3h_0$ and $\delta F_{Ez} = 0.2u_0^3(h_0/l_0)$.

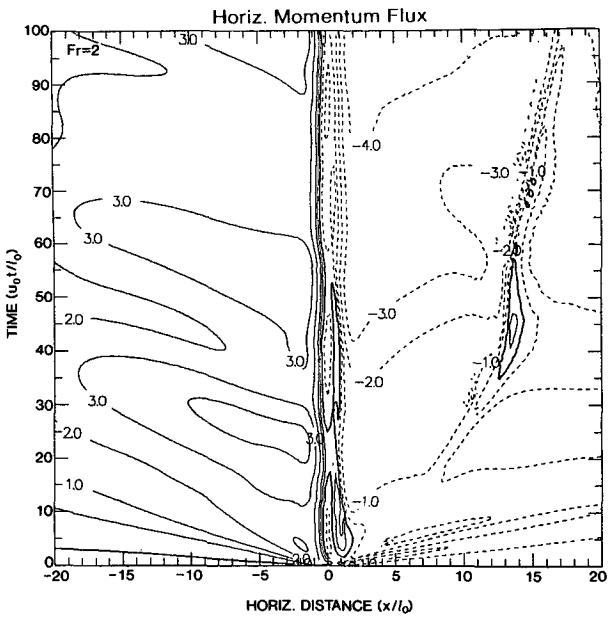

FIG. 23. As Fig. 20 except flux is calculated with pressure set to zero at the top of the control volume. Contour interval: $\delta\hat{F}_{ux} = 1.0u_0^2h_0$, except the +0.5 contour is also drawn.

$10\pi h_g$.) Typical upstream signal speeds deduced from the energy flux (Fig. 21) appear a bit slower, indicating a slight bias toward smaller vertical scales in the case of the energy spectrum. These estimates of far-upstream signal speed are much faster than the near-mountain transfer described in the previous subsection.

Estimating a signal speed, say c_ϕ, from contours of a quantity ϕ is based on

$$c_\phi = -\left(\frac{\partial\phi}{\partial x}\right)^{-1}\left(\frac{\partial\phi}{\partial t}\right). \qquad (13)$$

In the case of $\phi = \int (u - u_0)dz$, which we call $\hat{u}$, we may use (4) to replace the time derivative in (13) by the flow force convergence, $-\partial\hat{F}_{ux}/\partial x$, since the vertical fluxes are negligible. To check the consistency of the computed fluxes, we can then assume that the x scale of the ϕ disturbance is the same as that of its flux $\mathbf{F}_\phi$. Thus, we have $c_{\hat{u}} \approx \hat{F}_{ux}/\hat{u}$. In the case of Fr = 2, the perturbation in $\hat{u}$ is about $-0.4u_0h_0$, while $\hat{F}_{ux} \approx 2.0u_0^2h_0$. Hence, $c_{\hat{u}} \approx -5u_0$, roughly consistent with the foregoing graphical estimates. The energy data yield a similar result.

In Fig. 23, the flow force has been recomputed with an assumption of zero pressure perturbation along the top of the control volume. Since most of the flux contributed by the large vertical scales is due to the pressure integral, this calculation crudely isolates the contribution from shallow modes. The shallow modes appear to carry a large part of the wave breaking signal at the relatively slow speed of about $-1.0u_0$. On the other hand, comparison with Fig. 20 suggests that the shallow modes are *not* very important in the initial surge ($t < 5\tau_a$). A linear analysis by Baines (1988) shows that upstream signals due to small adjustments in (nondimensional) mountain height are dominated by long (columnar) waves with vertical structure resembling a stationary solution prior to the adjustment. The signal speeds are determined by the amplitude of the adjustment. Except for the effects of vertical dispersion, Baines's model may apply to the generation of wave breaking surges. From the present results, it seems much less applicable to the initial surge.

This recomputed flow force is especially informative in the case of the lee-broadened mountain, which causes almost no wave breaking transience. The time–distance plot of the modified flux for the lee-broadened mountain with Fr = 2, shown in Fig. 24, confirms the importance of the initial surge in establishing the quasi-steady state (much of the disturbance in the lee is not plotted because of the grid noise). It is clear that the upstream dynamics of this state do not depend on turbulence associated with wave breaking.

Details of the energy and momentum fluxes can be used to assess the effectiveness or consistency of an open lateral boundary condition. The condition used in the present model is based on the assumption that the flow of information is strictly outward across the boundaries. This may be inconsistent with actual solutions if they develop any inward flux. As it happens, a weak inward flux of perturbation energy generally appears within a narrow "window" at the upstream boundary, near the top of the hydraulic layer (cf. Fig. 19a). However, since the influx window shifts only a little during the simulation, there is not much danger that the wave

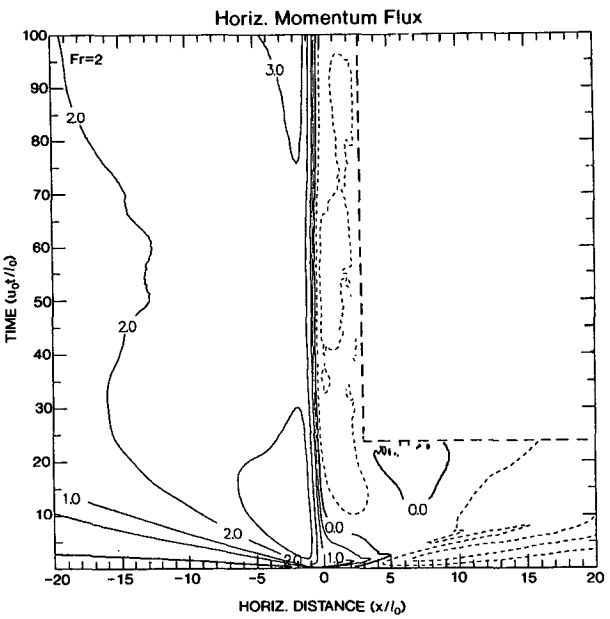

FIG. 24. As Fig. 20 but for lee-broadened mountain of Fig. 11.

advection boundary condition is imposing spurious values because of a reversal of signal direction.

It is riskier to simulate open lateral boundaries by inserting a sponge layer into a periodic model (e.g., Bacmeister and Pierrehumbert 1988). In order to develop and preserve the correct mean-flow modifications at the margins of the sponge, the width L_s and damping time T_s of the sponge must satisfy $L_s > c_0 T_s$, where c_0 is a conservative estimate of the signal speeds. In order to avoid reflections off of the sponge itself, there is the independent constraint that $T_s > \omega_0^{-1}$, where ω_0 is a conservative estimate of the wave frequencies. In the columnar disturbance, ω_0^{-1} can be quite large compared to the advection time τ_a. From these inequalities and the known phase speeds, we estimate that L_s should be at least an order of magnitude larger than l_0.

4. Discussion

The steady-state model introduced by Smith (1985) yields a prediction of the hydraulic-layer mass flux that nicely matches the present experimental result at the onset of permanent blocking. Unfortunately, Smith's model gives an unrealistic upper bound of Fr $\approx$ 1 on the range of mountain amplitudes supporting asymmetrical (high drag) steady states (as well as the wrong parameter dependence for total drag). In the true hydraulic problem (that is, in a strictly homogenous fluid), the mountain can be much higher for the same inflow depth. Denoting this depth as H_0 and defining $F \equiv \sqrt{g' H_0}/u_0$, where g' is the reduced gravity, we have from hydraulic theory (Long 1972; PW) that

$$\frac{h_0}{H_0} = 1 + \frac{1}{2} F^{-2} - \frac{3}{2} F^{-2/3}. \qquad (14)$$

When Smith's limiting value, Fr = $\mathrm{Fr}_{hb} = 3\pi/2$, is used for F, the above ratio is 49%, close to result of the stratified experiments at the blocking threshold. By contrast, Smith's solution for h_0 yields a maximum of only 21% of H_0. That the present time-dependent, stratified solutions are closer to the homogeneous steady-state model than to Smith's (steady state, stratified) model probably has a lot to do with boundary conditions. We consider first the upper, and then the upstream, condition.

The interval between the two occurrences of $\psi = \psi_h$ (the hydraulic-layer mass flux) in Fig. 14 contains the overturning circulation and mixed region (cf. Fig. 10). If the flow is steady and not very dissipative, such a circulation implies relatively high pressure at the upstream origin of the mixed layer, according to Bernoulli's principle (e.g., Moncrieff and So 1989). Yet Smith's solution assumes uniform pressure across the mountain at the undisturbed height of the hydraulic layer. Notice that the overturning becomes more active with increasing Fr in Fig. 15. Since the pressure anomaly varies as the squared speed of the circulation, and since the overturning speed can be comparable to u_0, the contribution to the momentum budget may be significant compared to the total drag in Smith's solution. The latter is $D = 1.1 u_0^2 H_0$ in the case of the deepest layer and highest terrain. (That the hydraulic disturbance is not fully isolated from the overlying atmosphere is also known from the existence of a residual wave train.)

The upstream boundary condition may be even more important. In the stratified experiments, the far-upstream hydraulic layer develops a weakly stratified sublayer beneath an anomalously stable capping layer. Smith and Sun (1987) studied this type of flow by introducing a homogeneous (neutrally stratified) layer at the ground in a generalization of Smith's (1985) model. Their calculations show that a single stratified layer is quantitatively like a homogeneous layer of roughly half the depth, capped by a thin stable layer containing the full buoyancy variation of the single stratified layer. This could explain why a capped, homogeneous layer supports roughly twice as high a mountain as Smith's stratified layer. In the stratified experiments, the homogeneous limit is approached without a significant lowering of the total hydraulic inflow depth.

It is not immediately clear how the alteration of the *velocity* profile affects this picture, or why Smith's value for H_0 remains valid as both the velocity and stratification profiles change. To see the effect of altering both stratification and velocity, we have generalized Smith's model using continuous upstream profiles. The solution procedure is described in the appendix. The velocity profile is chosen with u reduced at low levels and increased at high levels, with no change in the mean value u_0. For simplicity, we have retained the linear relationship between the streamfunction and the potential buoyancy, namely, $\psi = (u_0/N^2)b$. This keeps the vertical stratification everywhere proportional to the velocity. The potential temperature anomaly is negative throughout the modified layer, with a lower bound imposed by the constraint $u > 0$. Any initial relationship between ψ and b would be preserved in a linear model. The initial relationship is also preserved quite well in the finite-amplitude experiments.

The diagrams in Fig. 25 show the shape of the dividing streamline (top of the hydraulic layer) over a Gaussian mountain for two different upstream profiles. The velocity/stratification profile is shown at the left for each case. The values in the modified profile are reduced to 5% of the mean at the minimum level. Smith's upper bound, $H_0 = (3\pi/2)h_g$, is chosen as the upstream height of the layer for both the modified and uniform profiles. We see that altering the inflow profiles increases the terrain height by about 50% and yields a steeper cascade over the mountain. Both of these changes are realistic.

The maximum value of H_0 that allows steady asymmetrical states is only slightly increased by the strong alteration of upstream profiles. The bound on H_0 is ultimately due to the requirement that the terrain height h should be zero at two values of the interface displace-

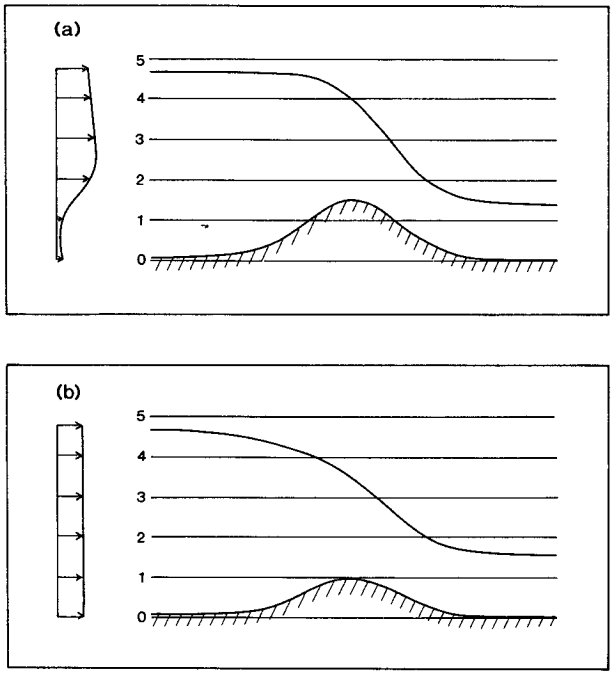

FIG. 25. Shape of the dividing streamline over a Gaussian mountain for the case of modified (top) and uniform (bottom) upstream wind and stratification. Vertical unit is h_g. Both streamlines start at the level $z = (3\pi/2)h_g$ far upstream. Mountain heights are $1.6h_g$ and $1.0h_g$ in the first and second cases, respectively. The depth of the downstream shooting layer is $1.3h_g$ in the first case and $1.6h_g$ in the second.

ment δ_c, namely, $\delta_c = 0$ and some $\delta_c < 0$. The satisfaction of this condition depends on the phase of the stationary internal wave at $z = H_0$ above the upstream foot of the mountain (there is no obvious interpretation in terms of a resonance). Apparently, this phase is not very sensitive to the particular velocity and stratification changes that we have introduced. It is easy to find realistic upstream profiles that allow even larger values of h_0/H_0 (as large as 49%, which is close to the experimental value at the blocking threshold) but for which no solution exists for $h(\delta_c)$ in a small neighborhood of $\delta_c = 0$. It is plausible that a small change in the upper boundary condition or in the conservation constraints could make these solutions continuous through $h = \delta_c = 0$ and therefore physically realizable. Under the present restrictions, the case depicted in Fig. 25 is the one that yields the highest terrain.[6]

As noted in section 3, the total drag in Smith's model has the wrong parameter dependence beyond the threshold for permanent blocking. It is worth trying to extend the model to account for the "orographic adjustment" that appears to take over beyond this threshold. If we retain Smith's assumption of zero vertical flux out of the hydraulic layer, the total drag can be equated to the difference in flow force across the mountain. Although there are a variety of structural changes occurring as Fr increases, we start as simply as possible by considering the flow force perturbation to be nonzero only on the downstream side, and by assuming that the downstream perturbation is due to the pressure anomaly of a mixed layer occupying the full depth H_0. The errors thus introduced are partially offsetting, but they grow considerably as Fr increases beyond the breaking threshold. The dimensional estimate becomes $D \approx (1/6)N^2H_0^3$. In units of $u_0^2h_0$, this is

$$D \approx \frac{1}{6}\left(\frac{H_0}{h_g}\right)^3 \mathrm{Fr}^{-1}. \tag{15}$$

Smith's result is obtained from (15) by replacing H_0 by $H_0 - H_1$, where H_1 is the depth of the shooting layer.

Next, we recall that orographic adjustment, as described in section 2, implies $H_0/h_g = H_b/h_g + \mathrm{Fr} - \mathrm{Fr}_b$, where H_b and Fr_b are blocking threshold values. Substitution into (15) yields

$$D_1 = \frac{1}{6}(\mathrm{Fr} + \alpha)^3\mathrm{Fr}^{-1}, \tag{16}$$

where $\alpha = H_b/h_g - \mathrm{Fr}_b$. Using Smith's upper bound for H_b and the experimental result $\mathrm{Fr}_b = 2.5$, we have $\alpha \approx 2.2$. The resulting dependence of D_1 on Fr is plotted in Fig. 17.

There is a qualitative improvement, but the large discrepancy remaining between D_1 and the model flux at $\zeta = 0$ suggests that the upstream changes are not unimportant in this range of Fr. In order to incorporate the change in upstream layer depth and flow force, we try inserting a linearly increasing function of Fr (Smith's upper boundary condition is retained because the residual flux is too small in Fig. 17 to account for the present discrepancy). Thus,

$$D_2 = \frac{1}{6}(\mathrm{Fr} + \alpha)^3(1 + \beta\mathrm{Fr})\mathrm{Fr}^{-1}. \tag{17}$$

This dependence is shown in Fig. 17 for the choice $\beta = 1/8$, which assumes that the previously neglected effects become comparable to the included effects when Fr = 8. The experimental values are obviously much better approximated with the extra factor.

5. Summary and conclusions

Long-term experiments for a range of Froude numbers fail to show any significant time-mean upstream flow transition corresponding to the transition to wave breaking over the mountain. The transience due to start-up and wave breaking (PW's "initial" and "wave-breaking" surges, respectively) can be distinguished

[6] The average upstream velocity in the simulated hydraulic layers can be as much as 20% smaller than the initial value, corresponding to an average N that is about 10% smaller. Renormalizing with these new averages (for a fairer comparison with the steady-state model) makes the experimental layer depth about 10% larger than indicated.

either by comparing solutions on opposite sides of the breaking threshold or by using highly asymmetric topography. Upstream influence, defined as permanent inflow alteration, is essentially due to the initial surge in both blocked and unblocked cases. The only significant time-mean upstream transition as a function of Fr appears at the threshold for permanent blocking, where orographic adjustment sets in.

Whereas the time-mean upstream surface wind falls off only gradually with increasing Fr, the structure of the *downstream* time-mean flow undergoes a sudden change at the wave breaking threshold. This change, well known from previous studies, establishes the upstream–downstream flow force difference needed to balance the enhanced mountain drag in the absence of any comparable vertical fluxes above the wave breaking. At high Froude number, flow force anomaly is mainly due to the pressure disturbance, rather than the flow speed perturbation. Near the breaking threshold, the low pressure in the lee is crucial, as all upstream changes are negligible. The small fraction of negative momentum that is transferred to the upper atmosphere is approximately the saturation value.

Unlike hydraulic flows, in which asymmetrical configurations are associated with upstream bores and rarefaction waves, upstream changes in the stratified flow do not become important in the momentum balance until well beyond the breaking threshold. This suggests that simple hydraulic theory will not provide a very useful analogy for *upstream* surges in the stratified model. Another reason for not pursuing the analogy is that the depth of the surges has been found to be at least 5 times the stationary wave scale. Viewed on this scale, the upstream environment contains nothing that could act in a manner analogous to a density interface or a reflecting lid. The multilayer hydraulic method of Baines (1988) for finite-depth stratified flows holds some promise for describing the upstream wave breaking signal, except for the effects of vertical dispersion.

Permanent blocking occurs for mountain heights greater than about half the upstream hydraulic-layer depth—a threshold reasonably well predicted by hydraulic theory if Smith's (1985) result is used for the upstream layer depth. Smith's model is for continuously stratified flows. Apparently, the mixture of theories succeeds because the height of the second node in a stationary, internal gravity wave is not very sensitive to changes in inflow velocity and stratification (for fixed mass flux and total buoyancy variation). The same vertical scale occurs in a theory involving partially resonant internal waves (Clark and Peltier 1984). Especially as it has been developed by Laprise and Peltier (1989), this theory clarifies the transition to high drag and the associated trapping of energy in the hydraulic layer. We have argued that it may also contain a partial explanation for the low-frequency upstream transience.

The low-frequency transience is associated with quasi-periodic wave breaking events or, in nonturbulent solutions, unsteepening events. The chief difference between the two, apart from the turbulence, is the sharply greater upstream penetration of the quasi-periodic signal in the breaking solutions, as also noted by Pierrehumbert and Wyman (1985) but interpreted by them as permanent alteration. The "plateaus" observed by Scinocca and Peltier (1989) in the wave drag history are due to the combination of wave breaking transience and a weak trend in downstream conditions. (We have minimized the relationship between wave breaking and upstream influence but could not rule out a connection, possibly involving wave breaking, between the downstream trend and *small* permanent adjustments upstream.)

The fact that upstream effects are permanent in Baines's (1988) finite-depth model suggests that the transience of the wave breaking signal in the semi-infinite atmosphere depends crucially on vertical dispersion. Steepening/unsteepening transience is probably due to internal absorption, reflection, and scattering of vertically propagating waves. These processes are difficult to analyze (e.g., through WKB theory) because the internal waves are nonlinear everywhere and because the mixed layer is deep and localized in the horizontal. In Long's solution, the refractive index,

$$l^2 = \frac{\partial b/\partial z}{(\partial \psi/\partial z)^2} \tag{18}$$

(neglecting the contribution from flow curvature), is largest in regions of reduced stratification ($\partial b/\partial z < N^2$) because ψ is a linear function of b. There may be a feedback between steepening and the implied absorptivity increase as l^2 increases over the mountain following start-up. Exactly what triggers the unsteepening events and the resulting radiative bursts is not clear, especially in the nonturbulent cases. As well as shear instability, the full mechanism may depend on the changing proximity of the overturning to the lower boundary and/or changes in the refractive index due to diffusion and flow curvature.

The problem of incorporating high drag into wave drag parameterizations splits into three issues: 1) identification of high drag conditions, 2) reformulation of the forcing function as these conditions become satisfied, and 3) application of the forcing to the resolved variables. Pierrehumbert (1986) and Shutts (1990) have suggested how to quantify the total drag on the atmosphere *above the hydraulic surface layer,* based on nonlinear models of such layers. There are also well-tested schemes for distributing this stress in the vertical (e.g., Palmer et al. 1986). The chief weakness of the latter schemes appears to be the assumption of zero internal reflection due to height- or time-dependent variations in refractive index. Other problems are due to the assumption of steady or two-dimensional forcing.

The present work relates to forcing *within the hydraulic layer.* This part of the wave drag parameterization effort will have an interesting new constraint: since global models do not resolve the trapping properties of the surface environment, high drag forcing must be applied on horizontal scales that do not excite vertically propagating gravity waves. This means that the horizontal forcing scale, say L_F, should be at least as large as the inertial distance: $fL_F/u_0 \geq O(1)$. Since high drag states have $Nh_0/u_0 \geq O(1)$, the condition is satisfied if $fL_F/(Nh_0) = O(1)$, that is, if the forcing is applied on the scale of the mountain's deformation radius. In typical global models, this could involve 2 or 3 adjacent grid points.

Trapping beneath a mixed-out critical level (as opposed to a steepening level) may also be amenable to parameterization, perhaps based entirely on numerical studies like that of Clark and Peltier (1984). Near the high drag threshold, most of the horizontal momentum flux occurs downstream. It may be possible to use this information in imposing the momentum sink. Some of the work by PW deals with transience associated with background rotation. An important step in the parameterization effort is to check whether the effect of rotation is the same in a model with resolved orography and one with parameterized orography at high Rossby number and high Froude number.

Acknowledgments. This work was inspired in part by a conversation with Richard Rotunno, who has been skeptical about the role of wave breaking in upstream influence. I am grateful for further helpful discussions with Isidoro Orlanski, Isaac Held, and Brian Gross. The figures were drafted by Catherine S. Raphael.

APPENDIX

High Drag Configuration with Modified Upstream Conditions

Here we generalize Smith's (1985) model to allow a wider variety of upstream flow profiles. In the hydrostatic, incompressible limit, Long's (1955) equation for steady, stratified flow in two dimensions becomes

$$\bar{u}\delta'' + (\bar{\gamma}/\bar{u})\delta = \bar{\eta}[(\delta')^2 - 2\delta'], \qquad \text{(A1)}$$

where $\delta(z)$ is the vertical streamline displacement, $\gamma = db/dz$, and $\eta = du/dz$. The overbar denotes upstream conditions evaluated at the undisturbed height $\bar{z} = z - \delta$, and the primes denote a derivative. Following Smith, we apply the boundary conditions

$$\delta = h \quad \text{at} \quad z = h \qquad \text{(A2)}$$

$$\delta' = 0 \quad \text{at} \quad z = H_0 + \delta \equiv H, \qquad \text{(A3)}$$

where h (the height of the terrain) and H_0 (the upstream height of the uppermost streamline) are specified constants. Since the horizontal velocity is $u(z) = \bar{u}(1 - \delta')$, the second condition is the same as $u = \bar{u}$ at $z = H$. The solution is physically meaningful only if u has the same sign everywhere.

When derivatives in (A1) are replaced by centered finite differences, discrete values of δ may be obtained successively as solutions of a quadratic polynomial equation. Either h or H must be treated as an eigenvalue. At the upper boundary, (A3) provides conditions on both δ and δ' in terms of H and H_0. Hence, it is easiest to integrate downward from $z = H$. The height of the terrain h is determined when (A2) is first satisfied; that is, when $\delta = z$.

The upstream mass streamfunction has the form $\bar{\psi} = u_0\bar{z} + \psi_1(\bar{z})$, with $\psi_1 = 0$ at both $\bar{z} = 0$ and $\bar{z} = H_0$ (so that the total mass flux is u_0H_0). We assume for simplicity that the potential temperature is proportional to ψ, as in the initial profiles for the time-dependent experiments. Thus, $\bar{b} = (N^2/u_0)\bar{\psi}$. This makes the coefficient, $\bar{\gamma}/\bar{u}$, in (A1) a constant. Based on the experiments, we try

$$\psi_1(z) = u_b \frac{H_0}{2} \log[1 + \alpha^2(z - z_c)^2] - (C_1 z + C_2), \qquad \text{(A4)}$$

where C_1 and C_2 are constants determined by the mass flux condition. The factor α determines the depth of the transition between the decelerated and accelerated layers of upstream flow. The height of the transition layer, and of the minimum potential temperature anomaly, is approximately $z = z_c$.

The solutions shown in Fig. 25 are for $H_0 = (3\pi/2)h_g$, $z_c = (\pi/2)h_g$, and $\alpha = (0.02h_g)^{-1}$. The profiles show u or γ as a function of z. The choice for u_b in Fig. 25a reduces the flow to nearly zero at its minimum value. Smith's solution, with $u_b = 0$, is shown in Fig. 25b. The alteration of the profiles increases the maximum terrain height by more than 50%.

Let δ_c be the displacement of the uppermost streamline; that is, $\delta_c = \delta(H)$. The relation $h(\delta_c)$ for each of the above solutions is shown in Fig. 26. In Smith's case, the physicality condition $h > 0$ for $\delta_c < 0$ is violated when the upstream depth H_0 exceeds $3\pi/2$. This bound on H_0 changes very little for the modified profiles. In

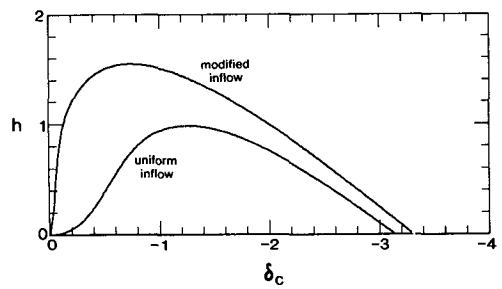

FIG. 26. The relationship $h(\delta_c)$ for the height of the terrain as a function of the displacement of the dividing streamline in the two solutions shown in Fig. 25.

general, $h(\delta_c)$ has several disconnected branches. Some of these allow higher terrain than the solutions in Fig. 26, but are unphysical in that they do not extend all the way to $\delta_c = 0$.

REFERENCES

Bacmeister, J. T., and R. T. Pierrehumbert, 1988: On high-drag states of nonlinear stratified flow over an obstacle. *J. Atmos. Sci.*, **45,** 63–80.

——, and M. R. Schoeberl, 1989: Breakdown of vertically propagating two-dimensional gravity waves forced by orography. *J. Atmos. Sci.*, **46,** 2109–2134.

Baines, P. G., 1979: Observations of stratified flow over two-dimensional obstacles in fluid of finite depth. *Tellus,* **31,** 351–371.

——, 1988: A general method for determining upstream effects in stratified flow of finite depth over long two-dimensional obstacles. *J. Fluid Mech.*, **188,** 1–22.

Benjamin, T. B., 1968: Gravity currents and related phenomena. *J. Fluid Mech.*, **31,** 209–248.

Clark, T. L., and W. R. Peltier, 1984: Critical level reflection and the resonant growth of nonlinear mountain waves. *J. Atmos. Sci.*, **41,** 3122–3134.

Durran, D. R., 1986: Another look at downslope windstorms. Part II: The development of analogs to supercritical flow in an infinitely deep, continuously stratified fluid. *J. Atmos. Sci.*, **43,** 2527–2543.

Garner, S. T., 1986: A radiative upper boundary condition adapted for *f*-plane models. *Mon. Wea. Rev.*, **114,** 1570–1577.

Kim, Y.-J., and A. Arakawa, 1990: Assessment of gravity wave parameterization schemes using a mesoscale gravity-wave model. Preprints, *Fourth Conf. on Mountain Meteorology,* Denver, CO, Amer. Meteor. Soc., 380–383.

Klemp, J. B., and D. R. Durran, 1983: An upper boundary condition permitting internal gravity wave radiation in numerical mesoscale models. *Mon. Wea. Rev.*, **111,** 430–444.

Laprise, R., and W. R. Peltier, 1989a: The linear stability of nonlinear mountain waves: Implications for the understanding of severe downslope windstorms. *J. Atmos. Sci.*, **46,** 545–564.

——, and ——, 1989b: The structure and energetics of transient eddies in a numerical simulation of breaking mountain waves. *J. Atmos. Sci.*, **46,** 565–585.

Lilly, D. K., and J. B. Klemp, 1979: The effects of terrain shape on nonlinear hydrostatic mountain waves. *J. Fluid Mech.*, **95,** 241–261.

Lindzen, R. S., 1981: Turbulence and stress owing to gravity wave and tidal breakdown. *J. Geophys. Res.*, **86,** 9707–9714.

Long, R. R., 1955: Some aspects of the flow of stratified fluids, III. Continuous density gradient. *Tellus,* **7,** 341–357.

——, 1972: Finite amplitude disturbances in the flow of inviscid rotating and stratified fluids over obstacles. *Annual Reviews in Fluid Mechanics,* Vol. 4, Annual Reviews, 69–92.

Miles, J. W., and H. E. Huppert, 1969: Lee waves in a stratified flow. Part 4: Perturbation approximations. *J. Fluid Mech.*, **35,** 497–525.

Miranda, M. A., and I. N. James, 1992: Non-linear three-dimensional effects on gravity-wave drag: Splitting flow and breaking waves. *Quart. J. Roy. Meteor. Soc.*, **118,** 1057–1081.

Moncrieff, M. W., and D. W. K. So, 1989: A hydrodynamic theory of conservative bounded density currents. *J. Fluid Mech.*, **198,** 177–197.

Orlanski, I., 1976: A simple boundary condition for unbounded hyperbolic flows. *J. Comput. Phys.*, **21,** 251–269.

Palmer, T. N., G. J. Shutts, and R. Swinbank, 1986: Alleviation of a systematic westerly bias in general circulation and numerical weather prediction models through an orographic gravity wave drag parameterization. *Quart. J. Roy. Meteor. Soc.*, **112,** 1001–1039.

Peltier, W. R., and T. L. Clark, 1979: The evolution and stability of finite-amplitude mountain waves. Part II: Surface drag and severe downslope windstorms. *J. Atmos. Sci.*, **36,** 1498–1529.

——, and ——, 1983: Nonlinear mountain waves in two and three spatial dimensions. *Quart. J. Roy. Meteor. Soc.*, **109,** 527–548.

Pierrehumbert, R. T., 1986: An essay on the parameterization of orographic gravity wave drag. *Proc. Seminar/Workshop on Observation, Theory and Modeling of Orographic Effects,* Vol. 1, Shinfield Park, Reading, UK, ECMWF, 251–282.

——, and B. Wyman, 1985: Upstream effects of mesoscale mountains. *J. Atmos. Sci.*, **42,** 977–1003.

Raymond, W. H., and H. L. Kuo, 1984: A radiation condition for multi-dimensional flows. *Quart. J. Roy. Meteor. Soc.*, **110,** 535–551.

Scinocca, J. F., and W. R. Peltier, 1989: Pulsating downslope windstorms. *J. Atmos. Sci.*, **46,** 2885–2914.

Shutts, G. J., 1990: A new gravity wave drag parameterization scheme for the unified model. Internal report, UK Meteorological Office, Bracknell, UK, 37 pp.

Smith, R. B., 1985: On severe downslope winds. *J. Atmos. Sci.*, **42,** 2597–2603.

——, and J. Sun, 1987: Generalized hydraulic solutions pertaining to severe downslope winds. *J. Atmos. Sci.*, **44,** 2934–2939.

Stoker, J. J., 1957: *Water Waves.* Interscience, 567 pp.